



# POLITECNICO MILANO 1863

## SSEO Lunar Reconnaissance Orbiter Reverse Engineering Project

Martínez Ferreira Daniel 10887367  
Scaramuzzino Alessio 10674740  
Scarpa Edoardo 10664387  
Torre Federico 10645141  
Valsecchi Andrea 10677064  
Zara Andrea 10698650



## **Abstract**

In this paper the Lunar Reconnaissance Orbiter mission is analyzed from the definition of its main objectives to the preliminary sizing of the spacecraft subsystems. The final goal is the identification of the mission requirements, through the process of reverse engineering.

In the first chapter of the paper, the mission goals, functionalities and main phases of the orbiter's lifetime are defined. Also the trajectory design has been analysed in order to validate the  $\Delta v$  breakdown.

In the following chapters, all the subsystems are analyzed and a preliminary sizing is performed for each case.

# Contents

<b>1 The Lunar Reconnaissance Orbiter Mission</b>	<b>1</b>
1.1 Introduction . . . . .	2
1.2 Objectives . . . . .	2
1.2.1 Main Objectives . . . . .	2
1.2.2 Extended Mission Objectives . . . . .	2
1.2.3 Drivers . . . . .	2
1.3 Functional analysis . . . . .	3
1.3.1 Functionalities & Phases . . . . .	3
1.3.2 Conceptual Operations & Phases . . . . .	3
1.4 Trajectory design . . . . .	5
1.4.1 Launch window . . . . .	6
1.4.2 Launch Vehicle and LRO deployment . . . . .	6
1.4.3 Mid Course Correction . . . . .	6
1.4.4 Lunar Orbit Insertion . . . . .	6
1.4.5 Frozen Orbit and Nominal Orbit . . . . .	7
1.4.6 Station Keeping and additional manoeuvres . . . . .	7
1.4.7 $\Delta v$ budget verification . . . . .	7
1.5 Payload . . . . .	9
1.5.1 Payload & Goals . . . . .	9
1.5.2 Payload & Phases . . . . .	9
<b>2 Propulsion subsystem</b>	<b>10</b>
2.0.1 Mission propulsion architecture . . . . .	11
2.0.2 Operation and phases related to the PS selection and architecture . . . . .	13
2.1 Sizing & configuration of propulsion subsystem . . . . .	14
2.1.1 Propellant masses & sizing . . . . .	14
2.1.2 Pressurant masses & sizing . . . . .	15
2.1.3 Thruster & Tank configuration . . . . .	15
2.1.4 Propulsion subsystem design comparison . . . . .	16
2.1.5 Mass & Power budget . . . . .	16
<b>3 Tracking Telemetry and Telecommunication subsystem</b>	<b>17</b>
3.1 TTMTC architecture . . . . .	18
3.2 TTMTC operations . . . . .	20
3.3 TTMTC sizing . . . . .	21
3.4 TTMTC budgets . . . . .	23
<b>4 Attitude and Orbit Control Subsystem</b>	<b>24</b>
4.1 AOCS Architecture . . . . .	25
4.2 Mission Modes . . . . .	25
4.2.1 Commissioning phase . . . . .	27
4.3 Sizing & Configuration of the AOCS . . . . .	28
4.4 Sensor Selection & Actuator Sizing . . . . .	28
4.4.1 Disturbances . . . . .	29
4.4.2 Sensor selection . . . . .	30
4.4.3 Actuator selection . . . . .	30
4.5 Power & Mass Budget . . . . .	31

<b>5 Thermal Control Subsystem</b>	<b>32</b>
5.1 TCS Architecture . . . . .	33
5.2 LRO Thermal Environment . . . . .	34
5.3 TCS Sizing . . . . .	35
5.3.1 Preliminary Study . . . . .	35
5.3.2 Single-Node Analysis . . . . .	36
5.3.3 Multi-Node Analysis . . . . .	37
5.3.4 Mass, Power & Data budgets . . . . .	38
<b>6 Electric and Power subsystem</b>	<b>39</b>
6.1 EPS Architecture . . . . .	40
6.1.1 Solar Array . . . . .	40
6.1.2 Power Subsystem Electronics . . . . .	40
6.1.3 Battery . . . . .	41
6.2 Mission phases . . . . .	41
6.3 Configuration & Sizing of the EPS . . . . .	41
6.3.1 Solar Array . . . . .	42
6.3.2 Battery . . . . .	43
6.4 Mass budget . . . . .	44
<b>7 Configuration</b>	<b>45</b>
7.1 Orbiter configuration . . . . .	46
7.1.1 Internal configuration . . . . .	46
7.1.2 External configuration . . . . .	46
7.2 Launcher interface . . . . .	47
<b>8 On-Board Data Handling subsystem</b>	<b>49</b>
8.1 OBDH Architecture . . . . .	49
8.2 OBDH Sizing . . . . .	51

# List of Figures

1.1	Relation Phases-Functionalities . . . . .	3
1.2	Early-stage ConOps . . . . .	4
1.3	Lunar Cruise and Orbit Injection ConOps . . . . .	4
1.4	Commissioning ConOps . . . . .	5
1.5	Routine operations manoeuvres timeline . . . . .	5
1.6	LOI 1 possible scenarios [4] . . . . .	6
1.7	First LOI cost for different Lambert's arc time of flight . . . . .	7
1.8	Lunar orbits comparison . . . . .	8
1.9	Nominal and NASA Horizon trajectory during LOI . . . . .	8
1.10	Relationship between the scientific objectives and the payload . . . . .	9
2.1	Propulsion System Fluid Schematic [6] . . . . .	11
2.2	Thrusters . . . . .	13
2.3	CAD model and physical parameters of the PS . . . . .	15
3.1	TTMTC subsystem architecture . . . . .	18
3.2	TTMTC components on LRO spacecraft [4] . . . . .	19
3.3	Ground Station facilities and locations [4, 30] . . . . .	19
3.4	Minimum $E_b/N_0$ with fixed BER . . . . .	21
3.5	Bandwidth for different data rates . . . . .	23
4.1	AOCS S/S architecture . . . . .	25
4.2	LRO mission modes [4] . . . . .	27
4.3	Attitude error disturbances [41] . . . . .	28
4.4	CAD model with the onboard instruments . . . . .	29
4.5	Sensor selection rationale . . . . .	30
5.1	Avionics module configuration . . . . .	33
5.2	Absorbed and radiated power in hot and cold scenarios . . . . .	37
5.3	Thermal resistance scheme for the hot scenario . . . . .	38
6.1	EPS architecture . . . . .	40
6.2	CAD model and physical parameters of the LRO . . . . .	42
6.3	Evolution of the Gimbal-1 movement with respect to the true anomaly [40] . . . . .	43
6.4	Evolution of the Gimbal-2 movement with respect to the $\beta$ angle [40] . . . . .	43
6.5	SA module design and parameters . . . . .	44
6.6	Battery model and design parameters . . . . .	44
7.1	LRO internal architecture . . . . .	46
7.2	LRO overall dimensions . . . . .	47
7.3	LRO folded configuration inside the Atlas V's EPF . . . . .	47
8.1	OBDH architecture . . . . .	49

# List of Tables

1.1	Lunar Reconnaissance Orbiter mission drivers . . . . .	3
1.2	LRO mission $\Delta v$ Budget . . . . .	5
1.3	Keplerian parameters of the LRO orbits around the moon . . . . .	7
1.4	Computed cost and relative error for the LOI burns . . . . .	8
1.5	<b>Relationship between payload and phases</b> . . . . .	9
2.1	PS architecture data [13] . . . . .	12
2.2	MONARC-90 main specifications [14] . . . . .	12
2.3	Aerojet, MR106L main specifications [15] . . . . .	12
2.4	Propellant mass and comparison between designed and real propellant consumption [6] . . . . .	13
2.5	Propellant properties . . . . .	14
2.6	Tanks masses, properties and operating conditions . . . . .	14
2.7	Pressure-fed system properties . . . . .	15
2.8	PS characteristics comparison . . . . .	16
2.9	Mass budget of the PS . . . . .	16
2.10	Power consumption [W] of the propulsion subsystem . . . . .	16
3.1	Installed antennas characteristics [27, 28] . . . . .	18
3.2	S-band and Ka-band system characteristics [4] . . . . .	18
3.3	Improvements in LOLA's data due to addition of high level positioning system accuracy [31] . . . . .	20
3.4	Priority files . . . . .	21
3.5	Ground station characteristics [30, 34] . . . . .	21
3.6	Sizing parameters [36] . . . . .	22
3.7	Sizing results . . . . .	22
3.8	Mass budget [kg] . . . . .	23
3.9	Power budget [W] . . . . .	23
4.1	Sensor and actuator performances [4] . . . . .	26
4.2	LRO mission modes [4] . . . . .	26
4.3	Instruments pointing budget [40] . . . . .	26
4.4	LRO inertia properties derived from sensors and actuators configuration . . . . .	29
4.5	Attitude disturbances evaluation . . . . .	29
4.6	Internal disturbance sources . . . . .	30
4.7	Actuators sizing results . . . . .	31
4.8	AOCS power and mass budget . . . . .	31
5.1	Instruments thermal coupling [40] . . . . .	33
5.2	Materials optical properties BOL (EOL) . . . . .	34
5.3	Temperature limits of payload instruments and components [40] . . . . .	34
5.4	S/C dimensions [52] . . . . .	35
5.5	Heat fluxes in hot and cold scenario [4] . . . . .	36
5.6	Internal dissipated power and total power absorbed in the analyzed scenarios . . . . .	36
5.7	Mononode results [53] . . . . .	37
5.8	Multi-nodal analysis results . . . . .	38
5.9	TCS mass budget [40] . . . . .	38
6.1	Solar Array degradation parameters [18] . . . . .	40
6.2	Battery Characteristics [18] . . . . .	41
6.3	Power consumption per mode, per system . . . . .	42

6.4	Battery Sizing Data . . . . .	43
6.5	Mass budget . . . . .	44
7.1	LRO internal & external components . . . . .	48
8.1	SBC characteristics and properties [59] . . . . .	50
8.2	OBDH hardware assembly [59] . . . . .	51
8.3	Frequency order of magnitude [Hz] . . . . .	51
8.4	Size and Throughput Estimates for Common Onboard Applications . . . . .	52
8.5	Size and Throughput Estimates for Operating System functions . . . . .	52
8.6	Total subsystem Size and Throughput estimate assuming 400% margin [36] . . . . .	52
8.7	ROM, RAM and Throughput comparison [59] . . . . .	52
9	CAD masses approximations . . . . .	v

# Chapter 1

## The Lunar Reconnaissance Orbiter Mission

### Change log

- **Sec 1.4** pp 5, 7: Format adjustment of Tables 1.2, 1.3.
- **Sec 1.4** pp 7, 8: Correction of Figures 1.7, 1.8a, 1.8b, 1.9b font size and style
- **Sec 1.5** pp 9: Correction of paragraph 1.5.2, addition of Table 1.5.

## 1.1 Introduction

The Lunar Reconnaissance Orbiter is a NASA mission launched on the 18<sup>th</sup> of June 2009. In conjunction with the Lunar Crater Observation and Sensing Satellite (LCROSS), it is part of the Lunar Precursor and Robotic Program (LPRP) in preparation for future manned missions to the moon [1].

The first launch date was fixed before the end of 2008 but as the spacecraft underwent testing in a thermal vacuum chamber, it was rescheduled for the first half of the following year. The launch date slid on June 18, 2009.

The LRO precursor missions provided medium resolution images, acquired to support the selection of Apollo and Surveyor landing sites. The coverage from the Apollo heritage involves only the equatorial regions. Information on new sites and resources is needed to enable sustainable exploration [2]. Therefore a mission to obtain a more refined description of the moon is needed.

## 1.2 Objectives

### 1.2.1 Main Objectives

The LRO main mission has a duration of 1 year, and its main objective is to conduct investigation targeted to prepare for and support future human exploration mission to the moon. During its mission the LRO shall:

- Locate potential resources, in particular:
  - Locate hydrogen and water near the lunar poles.
  - Study the mineralogy of the moon, namely the properties of the lunar regolith.
- Identify safe landing sites for in-situ resource utilization:
  - Provide high resolution images.
  - Characterize regions of permanent shadow and illumination.
  - Obtain the topography of the lunar surface.
  - Build a global morphology base map.
- Characterize the space environment on the lunar surface:
  - Analyze the Deep Space radiation.
  - Study the neutron albedo.
  - Examine the impact hazard on the surface.

### 1.2.2 Extended Mission Objectives

At the end of the main LRO mission, to take advantage of the remaining lifetime of the spacecraft, the scientific extended phase starts. The LRO extended phase mission focuses on different goals, which can be described as follows:

- Studying volatile materials, highly concentrated at the lunar poles, making these regions suitable as new landing sites for the following missions.
- Core, volcanics and tectonics, in order to understand the Moon's geology.
- Regolith studies as construction material on the Moon to sustain long-term human presence.

### 1.2.3 Drivers

The drivers of the mission, shown in Table 1.1, are those that express the physical and mechanical constraints of the mission (i.e. the starting point to properly design the satellite and the mission).

DRIVER	EXPLANATION
High Rate Data Downlink and Large On-board Data Storage	The high resolution imagery requires a high data downlink rate (100 Mb/s) and high capacity on-board data storage in order to store data when the link is not available.
High power consumption	According to the power needed from the satellite to perform the operations, the SA has to be designed properly. This choice is heavily influenced by the distance of the S/C from the Sun.
Delta-v capability	In order to perform the necessary LOI and the subsequent regular orbit adjustments, an independent propulsion system was required. Accommodation of the large fuel tanks was a defining characteristic of the overall spacecraft configuration.
Schedule & budget	For this Mission total budget is \$450M and four years to develop the mission from concept to launch. Strictly time requirements impose the use of available technologies with TRL 8-9.

Table 1.1: Lunar Reconnaissance Orbiter mission drivers

## 1.3 Functional analysis

### 1.3.1 Functionalities & Phases

The LRO mission is divided in five phases. In each one, the orbiter has to guarantee specific functionalities to accomplish the objectives of the mission. These functionalities can be summarized in reach the Moon, ground station, mission operations, S/C monitoring and S/C disposal.

Reach the Moon ensure that the satellite reach the correct orbit; ground station include all the functionalities for the communication of the satellite with ground; mission operations allows data acquisition and also accomplish the objectives of the mission; S/C monitoring detects the environment and avoids risks to the nominal behavior of the S/C; disposal ensures the end of life of the S/C.

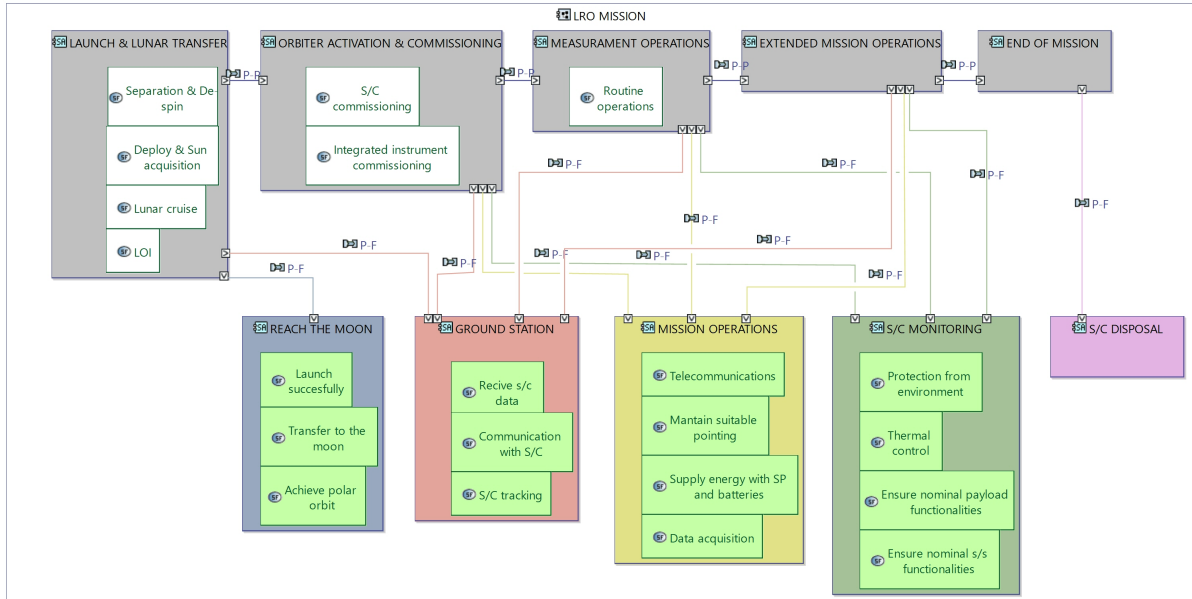


Figure 1.1: Relation Phases-Functionalities

### 1.3.2 Conceptual Operations & Phases

In this section a link between Conceptual Operations and Phases is presented.

The first phase of the LRO life is the *Separation and De-spin* phase, after the LTO injection. The S/C is released from Centaur upper stage with a residual angular momentum approximately equal to 15 Nms

[3] and its attitude is monitored by IMU and gyros. Therefore, the de-spin manoeuvre is performed by using RWs due to their momentum storage capability (from 90 to 120 Nms [4]) [5]. Instrument Survival heaters, Propellant heaters and Deployment heaters are enabled.

The following phase is represented by *Deployment and Sun acquisition*; the AOCS subsystem switches to *SunSafe mode*, which allows the S/C to start the acquisition of the Sun (exploiting the Sun sensors, the IMU and the RWs). The power is provided by the SA [4]. Furthermore, the TTMTTC subsystem starts the communications in its nominal condition (S-band, 16 kbps with omnidirectional antenna). After sun acquisition in order to empty the memory of the SBC, the transmission data-rate is increased to 300kbps. In Figure 1.2 the ConOps of the first two phases are reported.

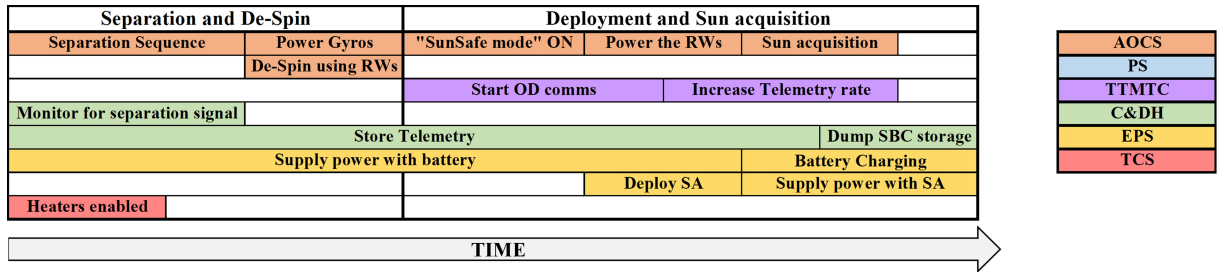


Figure 1.2: Early-stage ConOps

During the *Lunar Cruise* phase, HGA is deployed and control commands for PS configuration can be received [6]. Subsequently, two MCC burns are performed in order to fix the uncertainty on the trajectory after the release from the Centaur upper stage [7]; the AOCS control mode is switched to *Point mode*, in which the S/C can track any commanded inertial target [4].

The *LOI* phase is the most critical. In fact, four *LOI manoeuvre sequences* are performed in order to successfully reach the commissioning orbit. Each manoeuvre involves:

1. Configuring the propulsion system (enable the thrusters and catalytic bed)
2. Pointing the S/C
3. Transition to *Delta V mode* to point correctly the 80N thrusters.
4. Return to *point mode*

Due to *off-pointing* attitude, the communications are provided by the omni-directional antenna used in nominal condition.

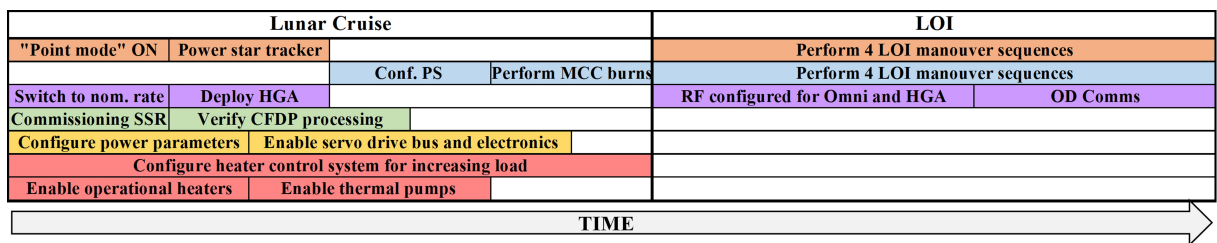


Figure 1.3: Lunar Cruise and Orbit Injection ConOps

During the *S/C commissioning* phase, the S/C subsystems functioning is checked and the S/C commissioned for the routine operations. Due to the fact that LRO is now orbiting around the moon, the battery is switched to *cycling mode*, providing power during eclipses and recharging during sunlight exposure.

During the *Integrated instrument commissioning* phase the S/C is prepared for the scientific operations. In order to reach the final orbit, the PS performs two burn sequences, similar to the ones during LOI phase.

When LRO reaches the target polar orbit around the moon, the *Routine Operations* phase starts. The operations that take place during that phase are summarized in Figure 1.5.

The 180deg *yaw manoeuvre* is performed in order to keep the Sun on the correct side of the S/C. This

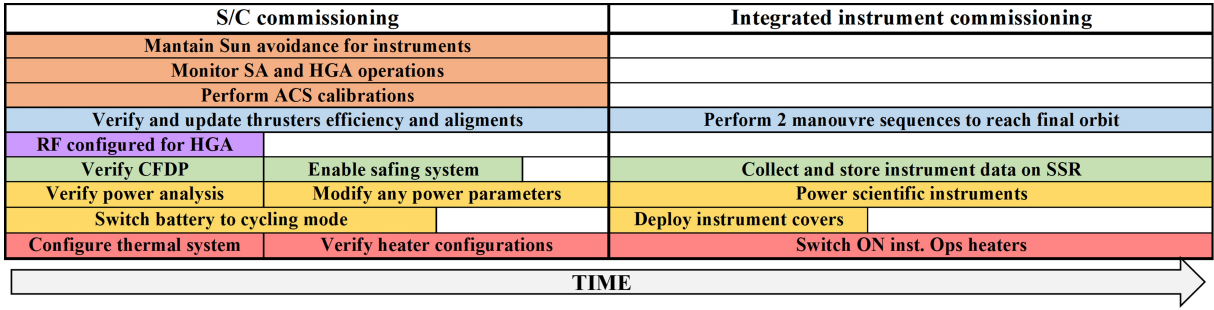


Figure 1.4: Commissioning ConOps

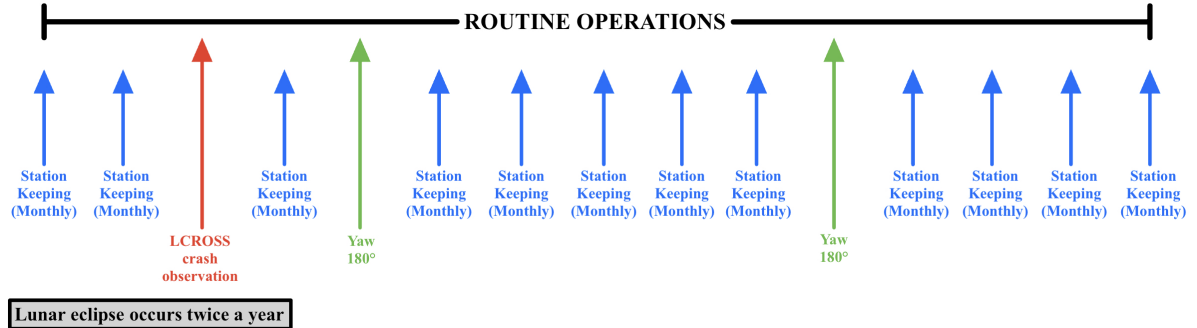


Figure 1.5: Routine operations manoeuvres timeline

manoeuvre occurs when the angle between the normal direction of the SA and the Sun-S/C line becomes close to zero [7]. The rotation is performed by the RWs, thus it may take a long time to complete (one orbit at most). The communications with the GS are performed with the omni-directional antenna because the HGA cannot be used during the manoeuvres.

Concerning the eclipse phase, if it lasts longer than 50 min, the orbiter enters in the *low power mode*, which means that all of the instruments are turned off, except for DLRE.

## 1.4 Trajectory design

The aim of this section is to carry out an in-depth study on orbital analysis related to the Lunar Reconnaissance Orbiter reversing the trajectory design and justifying the  $\Delta v$  budget adopted and reported in Table 1.2.

	$\Delta v$	Burn Time
<b>MCC 1</b>	28 m/s	-
<b>MCC 2</b>	4 m/s	-
<b>LOI 1</b>	567 m/s	38 min
<b>LOI 2</b>	185 m/s	12 min
<b>LOI 3</b>	133 m/s	12 min
<b>LOI 4</b>	41 m/s	12 min
<b>NOI</b>	50 m/s	-
<b>SK</b>	150 m/s	-
<b>Ext. Phase</b>	65 m/s	-
<b>TOTAL</b>	<b>1223 m/s</b>	-

Table 1.2: LRO mission  $\Delta v$  Budget

The numerical values reported in Table 1.2 make reference to preliminary mission analysis, in 2005 [7].

#### 1.4.1 Launch window

The main objective of the launch window study is to determine a departure date that allows to obtain a minimum energy transfer to the moon.

The launch energy required is a function of lunar phase and varies with a period of four to five days, due to the eccentricity of the Moon's orbit. There are two launch opportunities per day for a minimum energy direct transfer to the Moon: a short coast and a long coast [7].

Furthermore, science constraints impose other limits on the launch window. In order to identify regions of permanent shadow or lighting, these regions have to be observed in extreme lighting conditions [7].

The present constraints limit the LRO launch opportunities to one per day for a period of about three days every two weeks.

LRO spacecraft was launched at 21:32 UTC on 18 June 2009 from Cape Canaveral Launch Complex 41 [8], taking four and a half days to complete the journey.

#### 1.4.2 Launch Vehicle and LRO deployment

The launch vehicle adopted for the Trans-Lunar Injection (TLI) is the Atlas V-401 AV 020. This system allows to reach a Performance up to 3160 kg for TLI transfer and is capable of giving a characteristic energy  $C_3$  up to  $-2 \text{ km}^2/\text{s}^2$  [9].

The main requirements for the mission are a payload mass of 2810 kg and a characteristic energy  $C_3 = -1.91 \text{ m}^2/\text{s}^2$ . Both are fully satisfied [10].

Furthermore, the introduction of Atlas V eliminated the constant nutation time requirement related to the previous LV selection of a spin-stabilized three-stage Delta II [6]. In this way, it is possible to avoid any concerns due to nutation related to LRO's relatively large propellant mass fraction 46.87% [4]. In fact, it can be underlined that the total mass of the payload does not only include the LRO probe (1916kg wet mass) but also the LCROSS probe (700kg) [1].

After 45 min from the lift-off LRO is deployed by Atlas V-401 on a minimum transfer energy trajectory of  $194 \times 353700 \times 28^1$  [10].

#### 1.4.3 Mid Course Correction

LRO has only one planned mid-course correction manoeuvre, in order to correct for  $3\sigma$  launch vehicle errors.

LRO requires the velocity accuracy at launch vehicle separation to be within 3 m/sec. This uncertainty translates into a  $\Delta V$  budget for MCC-1 of 28 m/sec.

MCC-2 manoeuvre would only be required with a nearly  $3\sigma$  launch vehicle error and a nearly  $3\sigma$  performance of the propulsion system during the execution of MCC-1. MCC-2 would only require 4 m/sec to be back on target for lunar orbit insertion.

#### 1.4.4 Lunar Orbit Insertion

The lunar orbit insertion sequence consists of a large LOI-1 manoeuvre followed by a series of smaller LOI manoeuvres to place the spacecraft into the commissioning orbit. The LOI-1 manoeuvre is nominally 38 minutes long and provide the necessary  $\Delta V$  to allow LRO to be captured by the Moon's gravitational field. LOI-1 is planned to be such a long burn in order to minimize third-body effects. Two additional LOI manoeuvres are required to lower the apocentre and eventually circularize the orbit at 216 km. A final LOI burn is required to set the proper argument of periapsis and periselene altitude of the commissioning orbit. However, only one half of the thrust planned for LOI-1 is required to capture about the Moon (Figure 1.6), and there are different possible scenarios regarding the burn time [7]. In late June 2009 LRO successfully completed LOI manoeuvres without the necessity of exercising any contingency procedures, and achieved the planned quasi-frozen commissioning orbit.

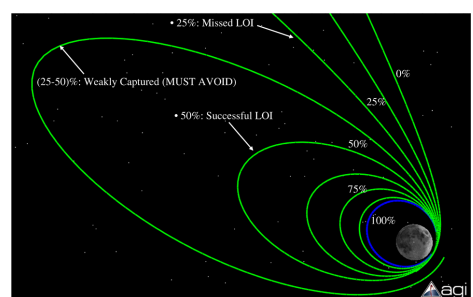


Figure 1.6: LOI 1 possible scenarios [4]

<sup>1</sup>Pericentre height [km] x Apocentre height [km] x Inclination [deg]

### 1.4.5 Frozen Orbit and Nominal Orbit

The non-spherical nature of the lunar gravity field cause a drift in eccentricity and argument of periapsis of the commissioning orbit. The condition is considered quasi-frozen since the eccentricity and the argument of periapsis are not fixed but merely bounded. The quasi-frozen orbit has a nominal eccentricity of 0.043 with a 216 km apocentre altitude. The average  $\omega$  is 270 deg, with periselene directly over the lunar south pole.

The frozen orbit can be maintained for many months, even years, without any station keeping (SK) manoeuvre. The frozen orbit will be used for the initial two-month-long instrument commissioning phase.

On 15 September 2009, the spacecraft transitioned to its nominal 2h period mapping orbit. Because of gravitational perturbations, the orbit eccentricity and argument of periapsis naturally evolve, and monthly station-keeping manoeuvres are necessary to preserve the mapping orbit. The eccentricity is  $0.0054 \pm 0.0019$  [8], and never more than 0.010, with the spacecraft altitude generally between 35 and 65 km.

### 1.4.6 Station Keeping and additional manoeuvres

An excess of  $\Delta V$  is reserved for the SK burns that maintain the orbiter on its nominal orbit, along with additional manoeuvres that may take place. SK is required because the eccentricity and argument of periapsis drift over time due to the non-spherical lunar gravity effect.

For the extended phase, it was predicted a  $\Delta V$  in order to reach a final quasi-frozen orbit. During this period a lower effort is required for SK but lower performance are granted during data acquisition.

Additional events comprise angular momentum desaturation from the RWs and, so, angular momentum relief burns are required. Furthermore a unique phasing manoeuvre to observe the LCROSS impact in October 2009 took place, which means that additional propellant is expended and must be taken into account for the budgeting. However the additional propellant cannot be related to a manoeuvre  $\Delta v$ , therefore is not reported in Table 1.2.

### 1.4.7 $\Delta v$ budget verification

The  $\Delta v$  budget for the main manoeuvres have been validated: the orbital parameters of LRO lunar transfer trajectory and lunar orbits, expressed in Table 1.3 are retrieved from the NASA Horizons System [11]. As represented in Figure 1.8a, the orbits that LRO follows before reaching the Commissioning orbit are 4, instead of 3 (separated by 4 LOI burns, Figure 1.9a) as predicted before the mission [7]. This variation is caused by a non-nominal result of the first LOI burn during the S/C's flight.

	<b>a [km]</b>	<b>e [-]</b>	<b>i [deg]</b>	<b><math>\Omega</math> [deg]</b>	<b><math>\omega</math> [deg]</b>	<b>Pericentre height [km]</b>
<b>Hyperbolic trajectory</b>	-6104.9	1.3395	89.80	6.45	330.24	334.42
<b>Orbit 1</b>	3382.0	0.4250	89.88	6.43	323.04	206.58
<b>Orbit 2</b>	2669.5	0.2729	89.81	6.47	322.74	203.06
<b>Orbit 3</b>	2207.8	0.1226	89.90	6.41	322.16	199.01
<b>Orbit 4</b>	1935.4	5.1759E-4	90.08	6.29	298.15	196.41
<b>Commissioning orbit</b>	1853.6	4.4735E-2	90.36	6.15	269.35	32.71
<b>Final orbit</b>	1788.1	5.4064E-3	89.90	4.95	160.67	59.80

Table 1.3: Keplerian parameters of the LRO orbits around the moon

In order to verify the predicted cost for the lunar orbit insertion, co-planar orbits and impulsive manoeuvres were considered as a first approximation. The hyperbolic trajectory and the first three orbits are considered also co-axial, with common pericentre coincident with the one of the orbit 1, where the impulsive manoeuvres are performed (Figure 1.8b). With this assumptions the computed total cost, reported in Table 1.4 is reasonably lower than the expected one.

The first manoeuvre differs the most from an impulsive manoeuvre, therefore it has been further analyzed: the keplerian elements of the followed orbit were propagated using the NASA Horizons System during the time frame of the first LOI burn with a one minute time step.

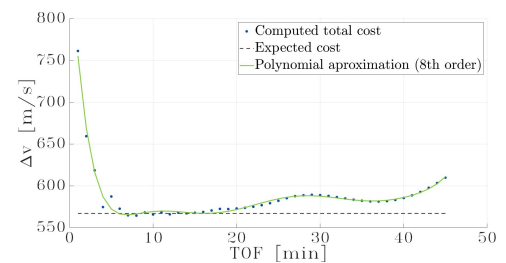


Figure 1.7: First LOI cost for different Lambert's arc time of flight

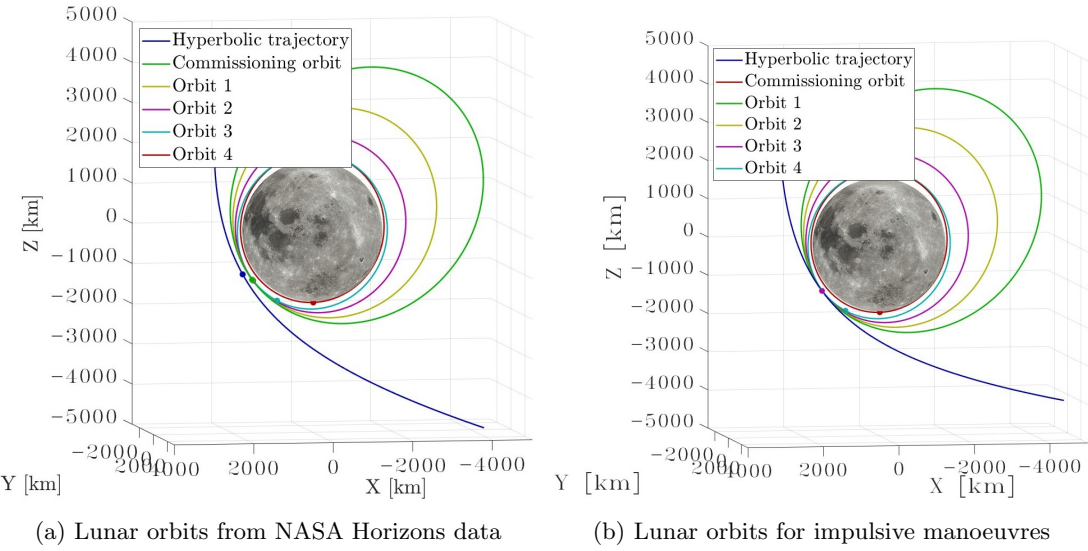


Figure 1.8: Lunar orbits comparison

To approximate the non-impulsive manoeuvre, a series of Lambert arcs are computed between two known consecutive positions (from Horizons data). The total burn cost, the sum of the many impulsive manoeuvres, that correspond to the  $\Delta v$  required to go from one arc to the next, is computed for different series of points, characterized by a different time of flight of the single Lambert's arc, as reported in Figure 1.7. It can be noticed that for a small time of flight the computed cost is much higher than the expected one. This is caused by the over-fitting that, with the perturbations, acts as a noise in the interpolation of the points with Lambert's arcs. Even for a larger time of flight the total cost is higher because the last Lambert's arc arrival point does not coincide with the actual ending of the real manoeuvre. Instead, in the middle the non-impulsive manoeuvre is approximated correctly. Moreover, from the analysis of the followed orbits data the first LOI burn appear to last 45 minutes instead of 38 minutes.

	Expected	Impulsive manoeuvres	Lambert's arcs
First burn cost	567 m/s	533 m/s $-5.96\%$	567 m/s $+0.033\%$
Total cost	935 m/s	878 m/s $-5.22\%$	912 m/s $-1.55\%$

Table 1.4: Computed cost and relative error for the LOI burns

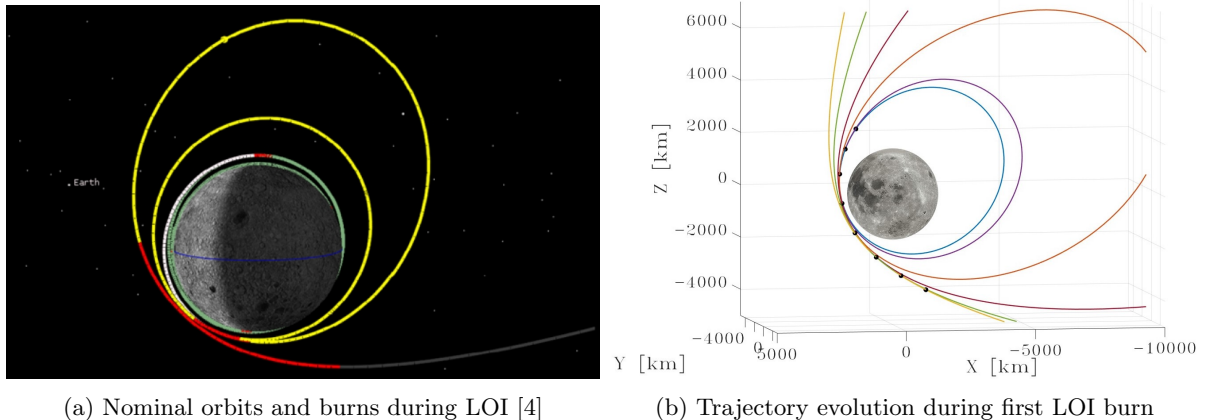


Figure 1.9: Nominal and NASA Horizon trajectory during LOI

The computed cost for the Lambert approximation is obtained taking the average value of the cases with a TOF between 7 and 16 minutes and is reported in Table 1.4. In fact, for all the points in the interval between 7 and 16 minutes the error is lower than 0.05%. The osculating orbits followed during the first LOI burn are represented in Figure 1.9b.

For the final manoeuvre, that moves the S/C from the commissioning orbit to the operations one, the verification of the cost is computed considering the nominal orbits: co-planar polar orbit, co-axial, the first 30x216km, the second 50km circular, joint by a Hohmann transfer. The obtained cost is 40 m/s, with an error of -17% reasonable with the simplifications taken into account.

## 1.5 Payload

### 1.5.1 Payload & Goals

To satisfy the mission objectives, the scientific instruments which comprise the payload must be designed/selected carefully, aiming to thoroughly cover every aspect of the goals without redundancy. Figure 1.10 shows the relationship between the scientific objectives, described in Section 1.2, and the instruments aboard the LRO [12].

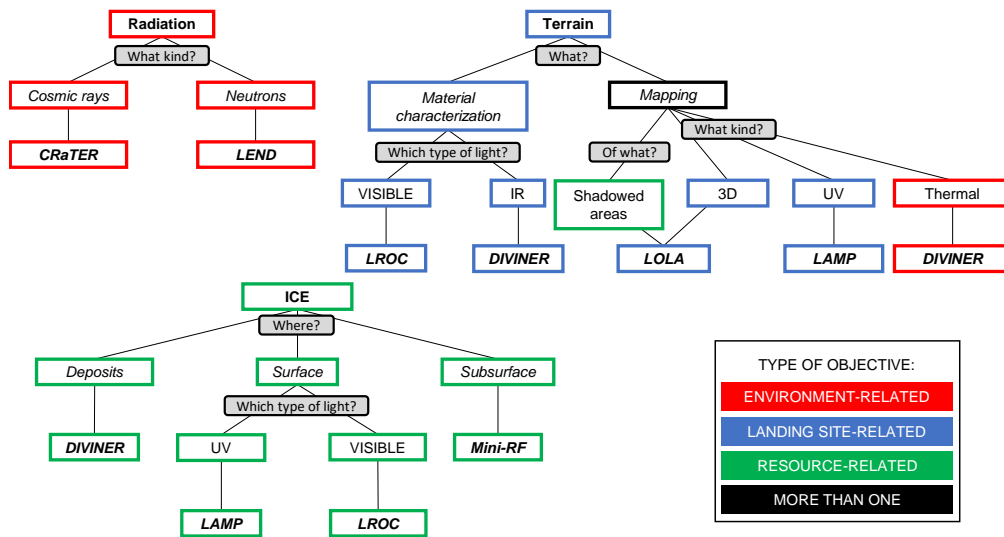


Figure 1.10: Relationship between the scientific objectives and the payload

### 1.5.2 Payload & Phases

The payload instruments are switched on during the instrument commissioning phase and work nominally after that phase is completed, as presented in Table 1.5. In addition, if the eclipse phase is predicted to last longer than 50 minutes, the S/C powers down its non-essential S/S and enters the low power mode. Therefore the payload instruments are switched off. When special scientific measurements are required (e.g. in coordination with LCROSS), off-nadir observations may take place, and these can involve different instruments depending on the kind of phenomena to be observed.

	Launch & Separation	Sun acquis.	Lunar cruise and insertion	Commissioning	Mesurments operations	Station keeping	Eclipse	Yaw manouvre	Off-nadir pointing
LROC	OFF	OFF	OFF	ON	ON	ON	OFF	ON	ON
LOLA									
CRaTER									
Diviner									
Mini RF									
LEND									

Table 1.5: Relationship between payload and phases

## **Chapter 2**

# **Propulsion subsystem**

In this chapter the Propulsion subsystem of the LRO is analyzed. After a brief study of the subsystem architecture, comprehending tanks, thrusters and feeding lines, a preliminary sizing is performed in order to understand the choices done during the real design.

### 2.0.1 Mission propulsion architecture

A pressure-regulated hydrazine monopropellant propulsion system is adopted, as shown in Figure 2.1.

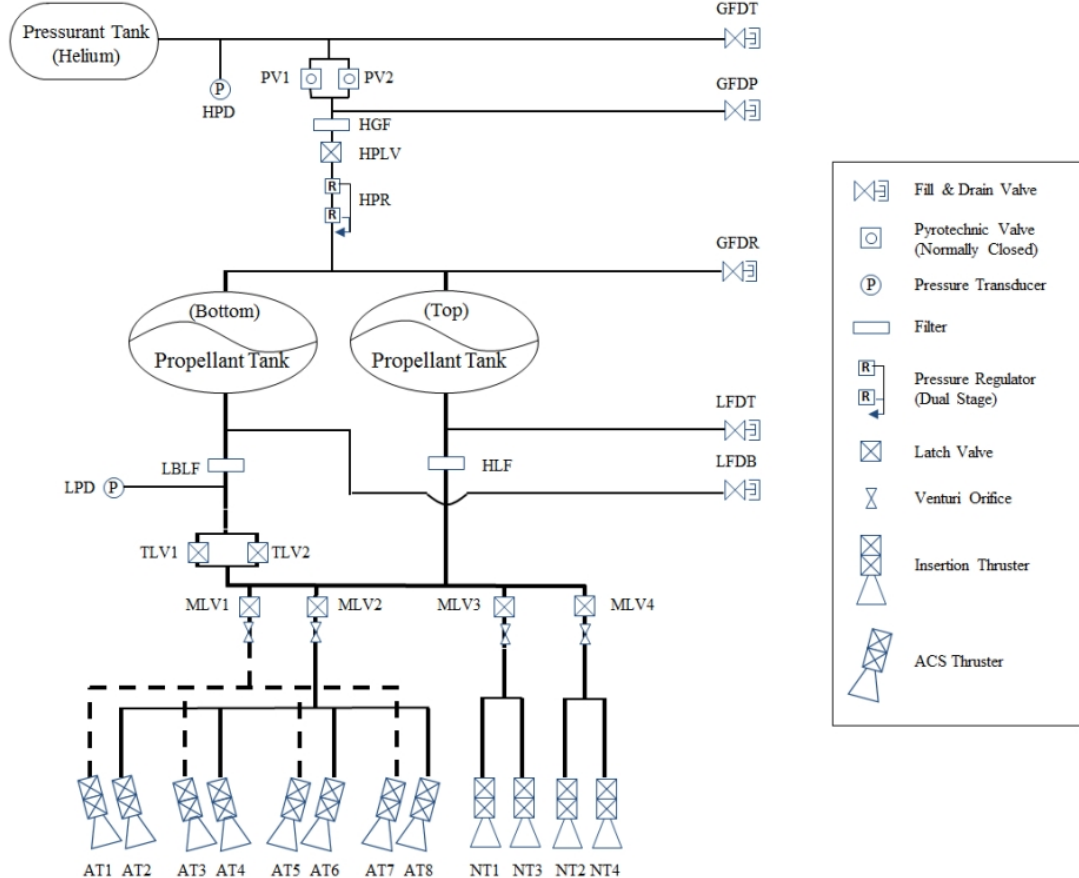


Figure 2.1: Propulsion System Fluid Schematic [6]

This design was selected mainly due to the strict schedule requirement because longer system integration times would be necessary for a bi-propellant architecture. Additionally, the wide application of this solution leads to a faster design and assembly. Hydrazine (Table 2.1) has been selected because of heritage, storability and high reliability. The low operating temperature of hydrazine monopropellant allows the chambers to be built using low cost materials and to be operated without cooling. Moreover, the architecture selected is much simpler (which usually implies greater reliability) than a bipropellant system, offering at the same time many of its advantages, such as easy on-off control and throttling. Therefore, the advantages of hydrazine mono-propellant are energetic simplicity, high TRL and moderate cost. A pressure-fed regulated system is chosen in order to avoid sloshing phenomena and to keep constant the pressure in the propellant tanks, and therefore the performances.

**Tanks** The project took advantage of the cancelled Hubble Robotic Servicing Mission (HRSM) exploiting its fuel tanks and its Attitude Control System [6].

These two tanks are made out of a Titanium alloy (Ti-6Al-4V) (Table 2.1) and they have a cylindrical body with girth-welded long oblate spheroids ends. Inside of each tank the separation between liquid propellant and pressurant gas is guaranteed by an elastomeric diaphragm, which can withstand a differential pressure of 689 kPa without damage when it is fully extended towards the propellant outlet [6]. The diameter of the tanks is 102 cm and the volume is capable of containing up to 894 kg of hydrazine, as required for the mission. Heaters, thermostats, and thermal sensors are installed on a thin metal shell surrounding each tank to monitor critical condition. The system contains a liquid filter downstream of each tank to avoid particulate contamination.

**Pressurization system** The pressure-fed configuration comprehends a pressuring gas contained in a composite overwrapped pressure vessel (COPV), which “communicates” with propellant tanks through pipes and an elastomeric diaphragm. The pressurant tank material choice is based on its durability, low production cost and minimum maintenance. The pressurant gas is Helium (Table 2.1) due to its near-ideal gas characteristic, cheapness and lightness. The COPV consists of a cylindrical body with hemispherical ends externally covered with a MLI blanket.

Propellant	Hydrazine	Pressurant	Helium	Tank material	Ti-6Al-4V	COPV
$\rho$ [kg/m <sup>3</sup> ]	1004	$\rho$ [kg/m <sup>3</sup> ]	0.166	$\rho$ [kg/m <sup>3</sup> ]	4430	1800
TRL	9	$\gamma$	1.667	$\sigma$ [MPa]	800	1040
		$R$ [J/kgK]	2077.3	No. tanks	2	1

Table 2.1: PS architecture data [13]

**Primary propulsion** The main usage of the primary propulsion installed onboard of LRO are the LOI burns. To quickly deliver the large amount of  $\Delta v$ , the insertion propulsion system is asked to provide greater than 160 N of thrust. Therefore, a bank of 90 N class thrusters are required. Four dual coil catalytic hydrazine thrusters (AMPAC, MONARC-90, Figure 2.2a) are installed, the main specifications are expressed in Table 2.2. In order to achieve single fault tolerance, four insertion thrusters are installed and divided in two manifold (A-side and B-side). This subdivision is adopted also for the secondary propulsion. The  $\Delta v$  required for LOI can be provided using only one thrusters manifold. The insertion thrusters present 90 degree-fixed nozzles, in order to minimize the occupied space onboard. They are located around the S/C x-axis on the aft face in a diamond configuration, with the center near the S/C CM, in order to avoid attitude control during LOI burns. However, after instruments placement, the CM is displaced leading to the usage of the ACS thrusters during the manoeuvres to compensate the undesired torque.

Steady State Thrust [N]	90 @ 235 psia	Specific Impulse [s]	232.1
Fed Pressure [bar]	5.5-27.6	Nozzle Expansion [-]	40:1
Valve Power [W]	75	Mass [kg]	1.12

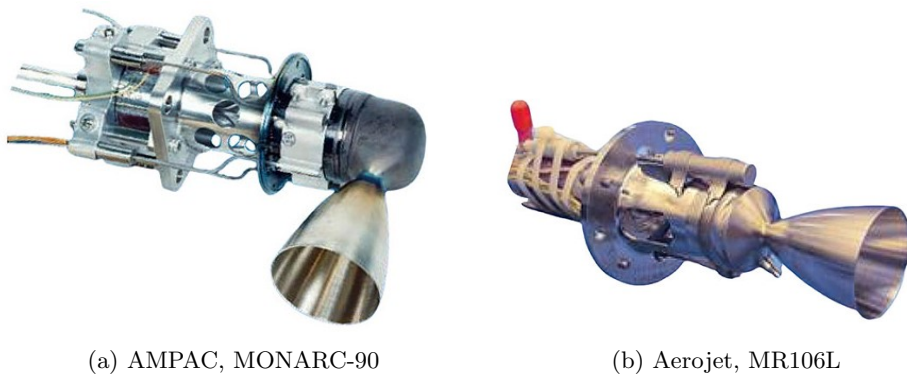
Table 2.2: MONARC-90 main specifications [14]

**Secondary propulsion** The main purpose of the secondary propulsion is to provide three axis stabilization and allow momentum unloading for the RWs. Therefore eight 22 N thrusters are installed, reaching the requirements with a single fault tolerance. The installed thrusters are Aerojet, MR106L (Figure 2.2b), whose main specifications are expressed in Table 2.3. The eight thrusters are divided in two manifolds that allows to insulate the other part of the system in case of a leakage. The desired performance are granted also with only one manifold active. The ACS thrusters are located in pairs, one thruster per manifold, at the four corners of the spacecraft’s aft face. They are canted 15 degrees towards the centerline in order to shift the thrust axis away from the CM, increasing the momentum during attitude control. All the 8 thrusters when operating in off-pulsing mode, provide a constant thrust of 176 N, sufficient for lunar capture in case of primary propulsion total fault.

Steady State Thrust [N]	34-10	Specific Impulse [s]	235-228
Fed Pressure [bar]	27.6-5.9	Expansion Ratio [-]	60:1
Valve Power [W]	25.1	Mass [kg]	0.59
Total Pulses [-]	120 511	Min Impulse Bit [Ns]	0.015

Table 2.3: Aerojet, MR106L main specifications [15]

**Valves** Two redundant pyrovalves (PV1-2) provide leak-free isolation for the launch phase. A high-pressure gas filter (HGF) was located downstream of the pyrovalves with one latch valve (HPLV) for isolation and two series-redundant pressure regulator (HPR). The system also contains five fill and drain valves for ground testing and loading of pressurant gas and propellant (GFDT, GFDP, GFDR, LFDT, LFDB). Downstream the bottom propellant tank, other two latch valves are installed (TLV1-2) in parallel, to reduce the pressure drop to the thrusters, with the aim of preventing transfer of propellant between tanks during launch. Moreover, each thruster manifold contained a latching isolation valve (MLV1-4) that isolate it at launch and in contingency situations.



(a) AMPAC, MONARC-90

(b) Aerojet, MR106L

Figure 2.2: Thrusters

### 2.0.2 Operation and phases related to the PS selection and architecture

The propulsion subsystem architecture is strictly related to the phase and operations of the LRO mission. The first PS activity is the subsystem configuration; this operation can be carried out after the deployment of the HGA (75 min after the separation) which allow the GS to send commands to the S/C. The configuration procedure consist of:

- Open each of the manifold latch valves separately (in order to separate the pressure surge events).
- Power the pressure transducer.
- Heat up the catalytic bed.
- Perform a short pulse on each ACS and LOI thruster (the duration of each pulse is calibrated according to the position of the trust vector respect to the CM).
- Turn off the catalytic bet heater after each pulse.

For each pulse, the telemetry data are compared to the expected behaviour.

The MCCs are the first manoeuvres that the PS must perform: these are achieved approximately one day after the LV separation. They are carried out by A-side ACS thruster bank in off-pulsing mode for  $\Delta v$  and attitude control. The costs of the MCCs are strictly related to the LV release accuracy. During the travel of LRO to the moon the propellant tanks need to remain unregulated, to avoid over pressurization above the MEOP (Maximum Expected Operating Pressure), caused by thermal effects.

In preparation to the LOI manoeuvres, the pyrovalves are switched on to open the high pressure

Manouvre	Designed propellant consumption [kg]	Real propellant consumption [kg]
<b>MCC</b>	26.4	1.2
<b>LOI-1</b>	444.9	414.4
<b>LOI-2</b>	121.8	67.0
<b>LOI-3</b>	81.3	67.1
<b>LOI-4</b>	24.1	55.8
<b>LOI-5</b>	Not designed	20.2
<b>TOTAL LOI MASS</b>	<b>672.1</b>	<b>624.5</b>
<b>Nominal Orbit Injection</b>	28.8	-
<b>Mission Orbit SK</b>	84.1	-
<b>Extended Mission</b>	33.5	-
<b>Momentum Unloading</b>	17.0	-
<b>Residuals</b>	15.4	-
<b>Unallocated margin</b>	20.9	-
<b>TOTAL</b>	<b>898</b>	-

Table 2.4: Propellant mass and comparison between designed and real propellant consumption [6]

feed system. Six hours before the scheduled LOI-1, an *engineering manoeuvre* is performed in order to check that the S/C is operating nominally in LOI configuration. This manoeuvre involved all the twelve thrusters. After the heating of the catalytic bed (45 minutes), the LOI-1 takes place: all the main thrusters fired for 40 minutes in order to give the required  $\Delta v$ , meanwhile the eight attitude thrusters

are set in *on-pulsing mode* to ensure attitude control during the manoeuvre. At the contrary, the others LOI manoeuvres do not required the same thrust level of the first one; therefore, only two of the insertion thrusters are needed to give the required level of thrust. The choice of thrusters to be used for the manoeuvres are based on the anomaly that the thruster would have encounter during the mission[6]. In the top part of the Table 2.4 is reported the comparison between the designed propellant consumption and real one after MCCs and each LOI manoeuvre. The LOI manoeuvres allowed the S/C to reach the Commissioning orbit. The PS performed the NOI manoeuvre in order to reach the final orbit. During the operational life, the the main function of the propulsion subsystem is to maintain the correct trajectory through the monthly SK manoeuvres and to desaturate the RWs whenever needed.

## 2.1 Sizing & configuration of propulsion subsystem

In the following sections, the propulsion system design, the system functions, the major requirements, and the propulsion subsystem budget will be discussed.

### 2.1.1 Propellant masses & sizing

The  $\Delta v$  and the masses considered for the sizing of the propellant tanks are reported in Table 2.5. The majority of the  $\Delta v$  is performed exploiting the primary propulsion. Moreover, both the 20N and the 90N thrusters present a comparable specific impulse. Therefore, based on these considerations, the  $I_s$  selected coincides with the one of the LOI thrusters.

Using Tsiolkovsky equation is possible to calculate the wet mass, than the propellant mass can be estimated. The margin applied to the propellant mass selection takes into account the real behaviour of the system such as: 3% of ullage, 2% for residual and 0.5% for loading uncertainty (MAR-MAS-080). Results are shown in Table 2.5.

DATA		MARGIN
Dry mass [kg]	1221.6	MAR-MAS-040 (20%)
$\Delta V$ [m/s]	1345.3	10%
$I_s$ [s]	232	-
Wet mass [kg]	2206	-
Mass of propellant [kg]	984.58	-
Marginated mass of propellant [kg]	1038.7	MAR-MAS-080 (5.5%)

Table 2.5: Propellant properties

For simplicity a spherical-shape tank configuration is considered. The volume of the propellant tanks is calculated by considering an additional 10% margin (according to MAR-CP-010). Knowing that for the 20N-class thrusters the chamber pressure is 13 bar, and for both the 20N and 90N thrusters the pressure in the feeding line is the same,  $P_c$  is considered to be equal for both systems, as seen in Table 2.6. The pressure in the tanks is defined considering two additional contributions:  $\Delta P$  injection and  $\Delta P$  feed starting from the pressure in the combustion chamber. Taking in account a pressure drop of 30% to calculate the  $\Delta P$  of injection, a lower operating pressure of the tanks is obtained when compared to literature data [16]. To avoid that, and also considering that the pressure drop is higher for small engines, the value is incremented to 80%. In this way a pressure, close to the operating one, is computed. For the propellant tank thickness sizing a safety margin taken from [17] is considered.

DATA		MARGIN
Internal voulme [ $m^3$ ]	0,5693	MAR-CP-010 (10%)
Thickness[mm]	2.304	300%
Tank mass [kg]	34.05	-
Full tank mass [kg]	1052.7	-
$P_c$ [bar]	13	-
$\Delta P$ injection [bar]	10.4	*
$\Delta P$ feed [bar]	0.5	-
$P_{tank}$ [bar]	23.9	-

Table 2.6: Tanks masses, properties and operating conditions

### 2.1.2 Pressurant masses & sizing

The model for the calculation of the pressurant gas mass is taken from [18], which led to an approximated value as shown in Table 2.7. For the mass of pressurant gas a 20% margin (MAR-MAS-090) is considered.

DATA		MARGIN
Mass of pressurant [kg]	5.784	MAR-MAS-090 (20%)
Internal volume [ $m^3$ ]	0.107	-
Cylinder thickness [mm]	11.425	50%
Spherical ends thickness [mm]	5.712	50%
Tank mass [kg]	16.237	-
Full tank mass [kg]	22.02	-
Operating pressure [bar]	330	-

Table 2.7: Pressure-fed system properties

The pressurant tank is a COPV realised in CFRP [19]. To define appropriately the characteristics of the tank, the mixture law [20, 21] is applied as follows:

$$\sigma_{composite} = \sigma_{fiber} \cdot \frac{V_{fiber}}{V_{tot}} + \sigma_{matrix} \cdot \frac{V_{matrix}}{V_{tot}}.$$

For the density, a typical value of  $1800\text{kg/m}^3$  is used [22]. For the pressurant tank thickness sizing a safety margin taken from [23] is considered.

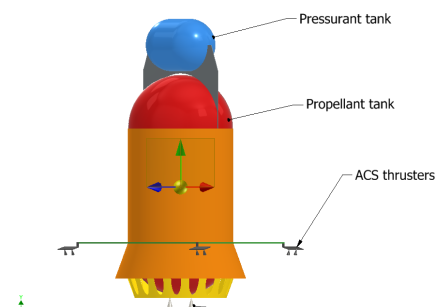
### 2.1.3 Thruster & Tank configuration

The tank configuration needs to take into account the choice of a pressure-fed system. The compactness of the system is driven by the following factors:

- Pressure losses
- Minimise heat exchange through exposed surfaces
- Minimise inertia (S/C easier to control)

Using a CAD software, a rough estimation of the tanks configuration has been modeled. The shape and volume of the tanks are defined considering the sizing in Table 2.6 and 2.7. As a first approximation it is possible to calculate the position of CM and the inertia moment of the tanks' configuration. The objective is to reduce as much as possible the Inertia moments of the orbiter such that the stability of the S/C is increased and also a minor amount of propellant is required to perform attitude maneuvers. To achieve that, the spacecraft is as compact as possible with the propellant carried along the center-line of the satellite.

In Table 2.3b the mass distribution properties and the CM coordinates of the approximate tank model (shown in Figure 2.3a) are summarised.



(a) PS CAD model

TANK CONFIGURATION		
Position of CM [mm]	Full	Empty
X	0	0
Y	543	452
Z	0	0
Mass moment [ $\text{kgm}^2$ ]		
I <sub>xx</sub>	591.779	147.066
I <sub>xy</sub>	0	0
I <sub>xz</sub>	0	0
I <sub>yy</sub>	159.413	56.298
I <sub>yz</sub>	0	0
I <sub>zz</sub>	600.871	156.159

(b) Center of mass and inertia moments of the PS

Figure 2.3: CAD model and physical parameters of the PS

As shown in Table 2.3b, the X and Z coordinates of the CM are equal to zero, which ensures the requirement of compactness [6]. In addition, looking at inertia moments between the full and empty tanks cases, the major and minor axes continue to be along the same geometrical axes.

#### 2.1.4 Propulsion subsystem design comparison

In Table 2.8 are reported the main characteristics of the PS, computed in the previous sections, compared with the real mission data. All the values are compatible or conservative estimations of the real

Propellant	Computed	Real	Error
Mass [kg]	1039	898	+15%
Tank volume [ $m^3$ ]	0.5693	0.4589	+24.1%
Tank mass [kg]	34.05	35.4	-3.8%
Pressurant			
Mass [kg]	5.78	3.3	+75%
Tank volume [ $m^3$ ]	0.1067	0.0819	+30.2%
Tank mass [kg]	16.24	12.7	+27.8%

Table 2.8: PS characteristics comparison

ones, while the pressurant mass differs significantly from the expected value. This is caused by the accumulation of the margins adopted for the previously computed quantities.

#### 2.1.5 Mass & Power budget

The mass budget of the entire PS, reported in Table 2.9, is composed by: the mass of the tanks, the mass of the pressurant gas and the mass of the thrusters. In addition a 10% margin is considered to take into account cables.

DATA	MARGIN
Mass budget [kg]	95.384

Table 2.9: Mass budget of the PS

In the Table 2.10 is shown a rough approximation of the power budget. For the propulsion subsystem the power consumption is given by the catalytic bed heaters [14, 15] and the valves. For the high pressure latch valve a consumption of 20 W is assumed, while for the low pressure latch valves it is fixed at 90 W. In addition the two manifolds work in parallel, as shown in Figure 2.1, therefore only one TLV and two MLV low pressure valves are considered. Since a single pressure transducer is expected to have a very low power consumption (<1W) [24], an excess estimation has been made. For each fill and drain valves the required power is taken from [25]. Both pyrovalves and filters are assumed to be negligible from the power consumption point of view. For the total power budget an additional margin is taken into account as defined in [26].

DATA	MARGIN	QUANTITY
<b>22N-Thrusters</b>	36,16	-
<b>90N-Thrusters</b>	100,8	-
<b>Valves</b>		
<b>High pressure latch valves</b>	20	-
<b>Low pressure latch valves</b>	90	-
<b>Pressure transducers</b>	< 1	*
<b>Fill and drain valves</b>	6	-
<b>Pyrovalves</b>	-	-
<b>Filters</b>	-	-
<b>Total power consumption</b>	1114.828	10%

Table 2.10: Power consumption [W] of the propulsion subsystem

## Chapter 3

# Tracking Telemetry and Telecommunication subsystem

### Change log

- **Sec 3.1** pp 19: considerations on frequency bands adopted.
- **Sec 3.3** pp 21, 22: BER correction, considered losses explanation; comment to bandwidth results; Table 3.7 values adjustment; Figure 3.5 modified.

In this chapter the TTMTTC subsystem of the LRO is analyzed. After a brief study of the subsystem architecture, comprehending antennas, amplifiers and GS, a preliminary sizing is performed in order to understand the choices done during the real design.

### 3.1 TTMTTC architecture

In Figure 3.1 the architecture of the LRO TTMTTC subsystem is represented, comprehending two different channels for communications with Earth: an S-band system that provides tracking, telemetry and commanding (TT&C) and an high data rate Ka-band system that works only in downlink for telemetry and science data transfer.

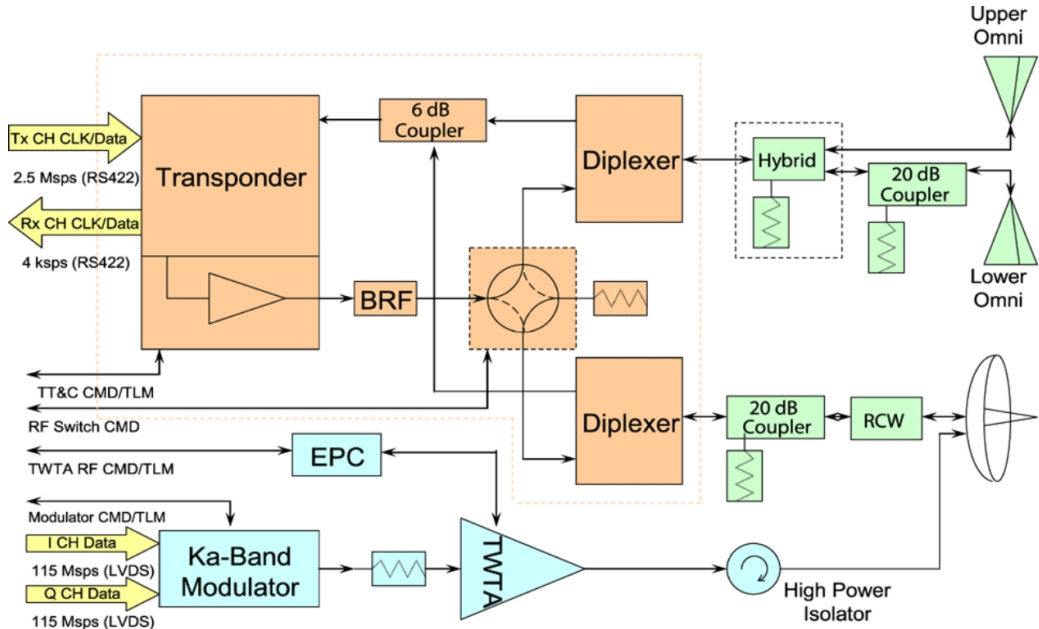


Figure 3.1: TTMTTC subsystem architecture

**Antennas** LRO mounts onboard one dual-axis high gain antenna (HGA), installed on a boom, that is required to point the selected ground station [27]. The gimbaled antenna also carries a co-boresight optical receiver telescope for laser ranging. Two omni-directional antennas (assumed Bi-conical) are mounted on opposite faces to cover all the directions around the S/C (Figure 3.2). The main characteristics of the antennas are reported in Table 3.1.

Antenna	Diameter [m]	Gain [dB]	Mass [kg]
<b>HGA</b>	0.75	43.49	3.62
<b>Omni</b>	-	5	0.25

Table 3.1: Installed antennas characteristics [27, 28]

Band system		Frequency	Datarate	Polarization	Power [W]	Mass [kg]
<b>S-band</b>	D/L	2271 ± 2.5 MHz	0.125-1093 kbps	LHCP (Omni), RHCP (HGA)	5.8 @ Diplexer	8.8
	U/L	2091 ± 2.5 MHz	4 kbps			
<b>Ka-band</b>	D/L	25.65 ± 0.15 GHz	100 Mbps	LHCP	41.9 @ TWTA output	8.4

Table 3.2: S-band and Ka-band system characteristics [4]

**Frequency bands** The S-band system consists of one Spacecraft Tracking and Data Network (STDN) compatible transponder, an S-band RF switch, the RF paths to and from the two omni-directional antennas and the S-band feed on the HGA. For the S-band, the uplink data rate is fixed at 4 *kbps*, while the downlink can be selected between 125 *bps* and 256 *kbps* (1093 *kbps* in direct modulation [1]).

In transmission, LRO can utilize either the Omni or the HGA, while in reception the path is selected from ground through the adopted polarization (LHCP for Omni path and RHCP for HGA path [4] as reported in Table 3.1). The use of omni-directional antennas leads to a lower carrier frequency in the transmission, therefore S-band is adopted **to limit the requested power during communications**. The Ka-band system also includes a Travelling Wave Tube Amplifier (TWTA) which is selected for having higher output power due to its better efficiency with respect to other amplifiers.

The Ka-band downlink is selectable on orbit and varies between 25 and 100 *Mbps* [29, 4]. The high frequency Ka-band is adopted to grant a large data rate, **which is needed due to the limited duration of the communication window and the large amount of data to be sent**. The Ka-band is less susceptible to interference but more prone to atmospheric attenuation, in particular in presence of precipitations (therefore a ground station located in a dry region is adopted).

**Comm Cards** The Comm-cards enable spacecraft communications with the ground, implementing the encoding and the modulation of the data stream. The S-Comm card is connected directly to the SBC via a 10 *Mbps* SpaceWire link. S-comm provides one stream up to 1093 *kbit/s* to the transmitter for Bi-Phase Shift Keying (BPSK) modulation onto the RF carrier. The Ka-Comm card is designed to accommodate a high-speed telemetry interface to Earth. The data stream is split into two streams for Offset Quadrature Phase Shift Keying (OQPSK) modulation. For both cases, data are encoded through the *concatenated encoding* (Convolutional and Reed-Solomon [1]) to respect the CCSDS recommendation[29, 4].

**Ground Stations** LRO makes use of a global network of S-band ground stations for nominal spacecraft tracking (at least 30 minutes per orbit) and one Ka-band station for downlink of all the stored instrument and spacecraft data (Figure 3.3). A commercial network, the Universal Space Network (USN), provides tracking with stations at Dongara, Australia; Kiruna, Sweden; Weilham, Germany; and South Point, Hawaii. The Doppler accuracy of the USN is  $\sim 1 \text{ mm/s}$  (one sigma) averaged over 10 s, which for the tracking time allocated permits LRO orbits to be determined to approximately  $\sim 10 \text{ m}$  radially and 300 m along-track and across-track [29, 4].

LRO can communicate with DSN ground station for early phases and emergency situations. The Ka-band station was specially built for the LRO mission and it is located at White Sands, New Mexico, USA (designated WS1).

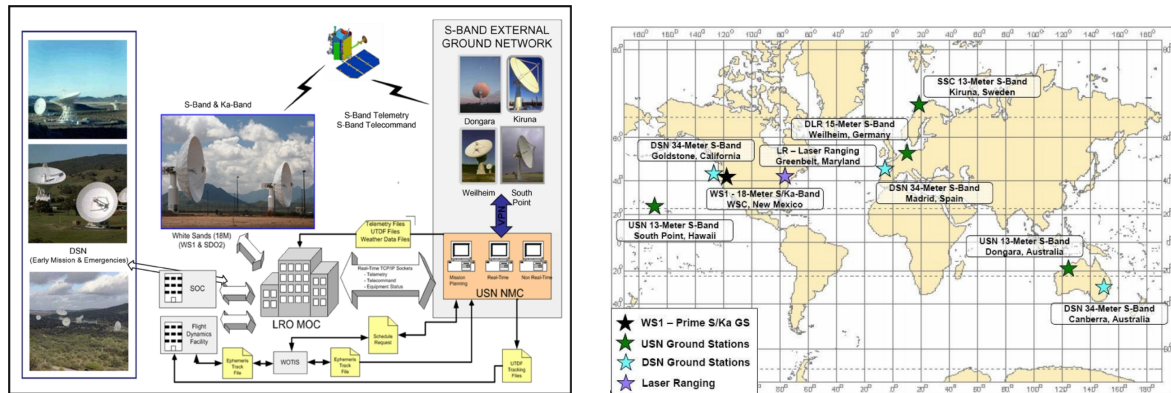


Figure 3.3: Ground Station facilities and locations [4, 30]

**Laser Ranging** The development of an high accurate ( $\sim 50 \text{ m}$ ) lunar global geodetic grid is one of the main objectives of the mission and the priority of the LOLA instrument [31]. For this reason, besides the instrument performance, an accurate positioning system for the S/C must be developed. In particular, the S/C must be tracked as precisely as possible when it is above the near side of the Moon so that, when it is on the lunar far side, the accumulated error is limited, avoiding the violation of the positioning requirement.

The base line tracking system for LRO is an S-band RF link which exploit doppler positioning system of the USN (Universal Space Network). However, the USN accuracy allow a resolution which is not compatible with LOLA requirement.

In order to achieve the accuracy requirement, *altimetric crossovers* from the LOLA instrument has also been used. *Crossovers* are point on the surface of the target body (the Moon in this case) where the S/C orbital trajectory cross. Therefore, where the Moon surface altitude is constant is possible to catch the positioning errors and correct them.

At the end, as *altimetric crossovers*, also laser ranging positioning system can be exploited. LR is a one-way time-of-flight measurement system which uses laser pulses to determine the range between a laser ranging ground station and LRO satellites. In fact, this positioning system consist of three components:

1. a small *receiver telescope* mounted on the HGA which capture the uplinked laser signal (**flight element**).
2. a fiber optic cable which routes the signal to LOLA instrument (**flight element**).
3. a network of laser ranging station on Earth (**ground element**).

In Table 3.3 are shown the accuracy improvement of the model thanks to LR positioning system.

<b>LOLA data products</b>	<b>S-band tracking alone</b>	<b>S-band + LOLA</b>	<b>S-Band + LOLA + LR</b>
<b>Global topography Accuracy / Resolution</b>	R: 10 m H: $\sim$ 300 m	R: 10 m H: $\sim$ 200 m	R: 1 m H: 50 m
<b>Polar topography Accuracy / Resolution</b>	R: 10m H: $\sim$ 300 m	R: 5 m H: 200 m	R: 0.1 m H: 25 m

Table 3.3: Improvements in LOLA's data due to addiction of high level positioning system accuracy [31]

## 3.2 TTMTTC operations

During the *Launch and Ascent phase* the TTMTTC subsystem of the LRO starts to be operative. Its data rate is set to 16 *kbit/s* exploiting LV telecommunications infrastructure, while the GS uses 4 *kbit/s* command rate to configure the orbiter. Once the separation sequence begins, the real time telemetry is off and the housekeeping and engineering telemetry data are only stored [32]. About 10 minutes after the LV separation, the omni-directional antennas are switched on and the 16 *kbit/s* data rate is restored. Subsequently, the data rate is temporarily increase to 128 *kbit/s* and the Laser Ranging operations are configured. The LDS (Local Data Storage) recorder starts data dumping.

In these following phases, the orbiter transmits through S-band, using the two omni-directional antennas installed on board. This solution allows the S/C to be connected with the Ground Segment also during the manoeuvres, when a specific pointing direction (as for HGA) can be difficult to maintain. In particular, the Space Network and the Deep Space Network shall provide S-band services during all the critical phases such as the LOI burns [33]. Once the commissioning orbit is reached, the orbiter performs a communication check-out through S-band and Ka-band. The HGA is configured within three weeks. During the *commissioning phase* if the S/C use the nominal S-band rate, the orbiter will be storing more data than it can downlink, therefore depending on the Ka-band usage, an appropriate data rate for the S-band shall be selected. For this reason the TTMTTC subsystem has the possibility to transmit in S-band from 125 *bit/s* to 256 *kbit/s* [1].

During the *routine operations phases*, all the S/C communications devices are operative. The HGA installed onboard allows to transfer large data volume in limited time windows, due to its high gain and strong directionality. The communication is performed only with the WS1 ground station. The critical point of the HGA is the pointing requirement, which is solved by installing a gimbals system over the two axes [27]. During a typical day in the monthly schedule the Ka-Band communication are limited to an average of 4 windows of 45 minutes [4].

The data volume required for the science phase is extremely high due to the data type provided by the instruments. HK and scientific data to be transferred to ground during WS1 Ka-band communication are queued for downlink based on priority as shown in table 3.4. Once the files are successfully downlinked, they are deleted from the recorder.

During the daily operations, the orbiter will pass in the Earth visibility window about once a orbit. It is a crucial event, therefore a specific sequence of event is performed:

- In the interval before the passage, the HGA points towards the selected GS and, based on WS1, visibility, the appropriate transmission band is selected.

- During the passage the S/C downlink event messages, HK and Measurement data and perform an Health and safety check [32, 33].
- Post passage the S-band and Ka-band telemetry are switched off.

In total during the passage in WS1 visibility the S/C shall be able to transmit around  $460 \text{ Gbits/day}$  [4].

<b>I</b>	Contingency Files
<b>II</b>	LEND
<b>III</b>	CraTER
<b>IV</b>	S/C HK
<b>V</b>	DLRE, LOLA, LAMP
<b>VI</b>	LROC
<b>VII</b>	Mini-RF, debug

Table 3.4: Priority files

### 3.3 TTMTTC sizing

In order to validate the retrieved data on LRO TTMTTC, subsystem a preliminary analysis is performed. In all the studied scenarios the S/C is located around the Moon, at a distance of  $384400 \text{ km}$  from Earth. The two frequency bands are analyzed in different conditions, as reported in table 3.7. To perform the study, one ground station for each scenario is chosen, considering the most stringent specifications (Table 3.5).

Case	Ground station	Antenna diameter [m]	Gain [dB]	Noise T [K]	$SNR_{min} [\text{dB}]$
Ka-band	White Sands 1	18.3	71.24	250	10
S-band	Dongara	13	47.21	150	10

Table 3.5: Ground station characteristics [30, 34]

The encoding is a process that consist in adding extra bits in the data stream at the transmitter. These bits enable the receiver to detect and correct for a limited number of bit errors which might occur in transmission because of noise or interference. The extra error correction bits increase the bit rate, and hence the transmission bandwidth. The encoding selected for both bands is the Concatenated encoding (Convolutional + Reed Solomon), whose *Spectrum utilization* parameter is reported in Table 3.6. Concerning the modulation, the Ka-band system adopts a OQPSK modulation, while the S-band system exploit a BPSK modulation.

The *Spectrum utilization* parameters are reported in Table 3.6. Binary Phase Shift Keying (BPSK) consists of setting the carrier phase at  $0^\circ$  to transmit a binary 0, and setting the phase at  $180^\circ$  to transmit a binary 1, therefore a relation 1:1 subsist. It is selected because it represents an easier solution to implement, exploited for a relatively low data rate. On the other hand, Quad Riphased Phase Shift Keying (QPSK), takes two bits at a time to define one of four symbols (2:4). The adopted coding significantly reduces the  $E_b/N_0$  requirement, which reduces the required transmitter power and antenna size, or increases the link margin. For all the analyzed cases a  $BER = 10^{-9}$  has been assumed [35]. From graph reported in Figure 3.4 the minimum link budget is obtained and reported in Table 3.6 (assuming constant  $E_b/N_0$  below  $BER = 10^{-7}$ ). The value assumed for the Ka-band system is conservative because it is parameterized over the modulation and does not include the encoding effects, which leads to a lower outcome. To ensure the functioning of the system

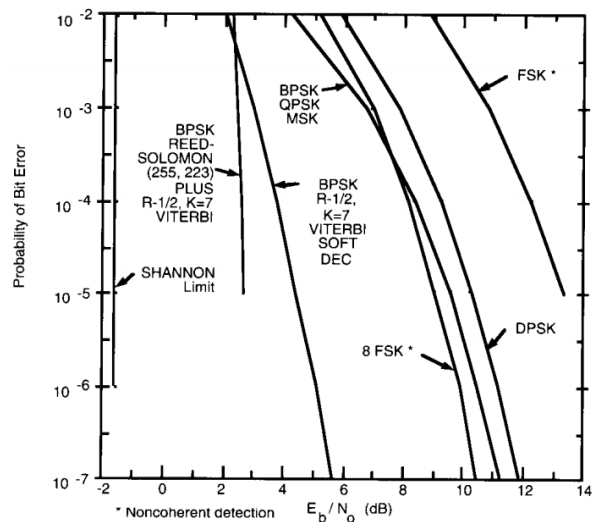


Figure 3.4: Minimum  $E_b/N_0$  with fixed BER

the  $E_b/N_0$  value shall be 3 dB higher than the minimum threshold. For the Ka-band system a higher modulation index is assumed, according to the larger data rate [18], while for the S-band, the  $\beta_{mod}$  is lower, as reported in Table 3.6.

Case	$\alpha_{enc}$	$\alpha_{mod}$	$(E_b/N_0)_{min}$	$\beta_{mod}$
Ka-band	2.29 symbol/bit	2	10 dB	78°
S-band	2.29 symbol/bit	1	3 dB	60°

Table 3.6: Sizing parameters [36]

The considered ground station temperature (Table 3.5) is lower for the S-band GS, according to [34]. In order to make the analysis more robust various losses are considered: atmospheric losses obtained from the graph in [18], accounting only for dry air, losses due to precipitation are neglected (given the position of the ground stations); cable losses, assumed to be 1 dBW; space, pointing and modulation losses.

Case	Datarate	Frequency	Symbol rate	$E_b/N_0$	SNR	$B_{min}$	$B_{max}$
Ka-band D/L	100 Mbps	25.65 GHz	114.5 MSymbol/s	19.4 dB	14.3 dB	16.1 MHz	21.8 MHz
S-band D/L (HGA)	256 kbps		586.2 kSymbol/s	14.1 dB	16.3 dB	89.5 kHz	190 kHz
S-band D/L (Omni)	16 kbps		36.6 kSymbol/s	8.73 dB	10.2 dB	6.48 kHz	3.43 kHz
S-band U/L	4 kbps	2091 MHz	9.16 kSymbol/s	11.9 dB	13.8 dB	1.47 kHz	-

Table 3.7: Sizing results

The minimum bandwidth ( $B_{min}$ ) in Table 3.7 is computed reversing the *Shannon's Theorem* for digital signals, where the data rate R takes into account the modulation and encoding, and the  $E_b/N_0$  value is computed from the transmitted power. The maximum bandwidth ( $B_{max}$ ) is obtained from the minimum SNR requirement of the receiver (Table 3.5) with a 3 dB margin.  $P_{carr}$  takes into account the received power and the power modulation losses.

$$B_{min} \log_2 \left( 1 + \frac{E_b}{N_0} \cdot \frac{R}{B_{min}} \right) - R = 0 \quad 10 \log_{10}(B_{max}) = P_{carr} - N_0 - SNR_{min}$$

The HGA is able to operate both in Ka-band and S-band nominal conditions because it respects the constraints on  $Eb/N0_{min}$  and  $SNR_{min}$  (Table 3.5, 3.6, 3.7). The omnidirectional antenna, instead, does not satisfy the minimum  $SNR$  (considering the 3 dB margin), in fact the minimum bandwidth exceeds the maximum one. Therefore a more detailed analysis is carried out in order to compute a minimum required power for the transmission. In Figure 3.5 the  $B_{max}$  value marks the feasible region while the  $B_{min}$  values are represented by the black curves parameterized over the data rate  $R$ . The SNR is compatible with the receiver requirements for at least one bandwidth value if  $B_{min}$  is inside the feasible region. As shown in Figure 3.5a, with the HGA, increasing the transmitter power to 12.5 W, also the non nominal condition of datarate 1093 kbps can be reached. Instead the omni-directional antenna cannot operate in the 16 kbps nominal data rate; a higher power is requested to transmit at larger data rates than 2 kbps (Figure 3.5b). In the U/L scenario some different assumptions are considered with respect to the D/L one, in particular:

- The receiver is the omni-directional antenna therefore the beamwidth is fixed at 45° [36]
- A different value of  $SNR_{min}$ , compatible with the onboard antennas should be assumed, but in this analysis the same 10 dB value is considered.
- $BER = 10^{-5}$  is required in uplink [35].

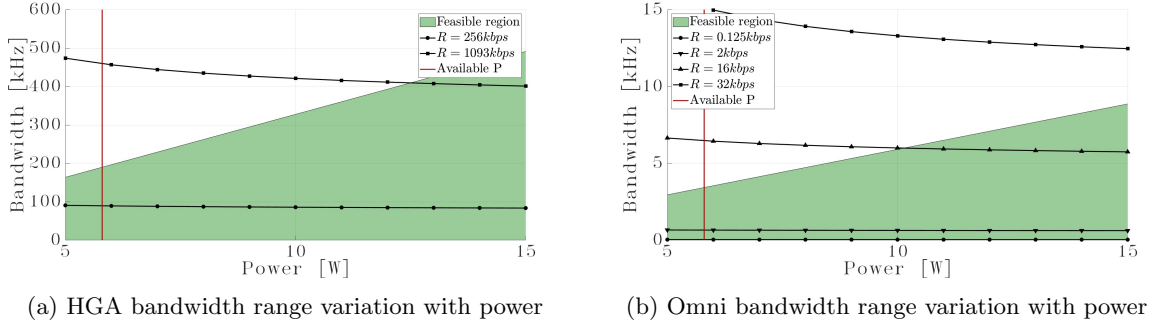


Figure 3.5: Bandwidth for different data rates

### 3.4 TTMTTC budgets

The mass budget of the TTMTTC subsystem is reported in Table 3.8. The S-band and Ka-band systems mass are taken from [4], while the HGA mass is estimated from statistical data knowing its diameter:  $m_{HGA} = 2.89 \cdot D_{HGA}^2 + 6.11 \cdot D_{HGA} - 2.59$  [18]. The mass of the two Omni is assumed from a similar model [28], taking into account the technology evolution. A 10 % margin is added to take into account cables and extra masses (Figure 3.1).

Component	Mass	Number	Margin
<b>HGA</b>	3.62	1	-
<b>Omni</b>	0.25	2	-
<b>Ka-band System</b>	8.4	1	-
<b>S-band System</b>	8.8	1	-
<b>Total</b>	<b>23.45</b>	-	<b>10 %</b>

Table 3.8: Mass budget [kg]

To compute the power budget, reported in Table 3.9, the input power is retrieved from the output of TWTA and diplexers [18]. For the S-band system a SSA is assumed, typically used for low power architectures. The values are retrieved graphically [18] and not analytically, therefore a 10% margin has been considered.

Component	Output	Efficiency	Input	Margin
<b>Ka-band system</b>	41.9	55.9 %	75	-
<b>S-band system</b>	5.8	16.7 %	35	-
<b>Total</b>	-	-	<b>121</b>	<b>10 %</b>

Table 3.9: Power budget [W]

## Chapter 4

# Attitude and Orbit Control Subsystem

### Change log

- **Sec. 4.2** pp 26: further explanation of the observing mode, Table 4.3 with instruments pointing budgets.
- **Sec. 4.2.1** pp 27, 28: Commissioning phase operations explanation, additional sources of error: Diviner calibration, RW zero-crossings and SA articulation. Addition of Figure 4.3.

The Attitude Control System (ACS) controls the pointing of the LRO spacecraft, specifically it compensates disturbances and keeps the orbiter in the desired attitude. In this section the rationale behind the sizing and selection of sensors and actuators is discussed.

## 4.1 AOCS Architecture

The primary objective of the AOCS is to provide pointing knowledge to within 30 arc-sec per axis (at  $3\sigma$ ) and to control the orbiter to within 45 arc-sec accuracy (at  $3\sigma$ ). To do this, the S/C is equipped with 10 CSS, 1 three-axis laser ring gyro MIMU, 2 star trackers, 4 RWs and the PDE which controls the use of the NEAs and the NSI to open thruster isolation valves and deploy the SA and HGA [37]. The AOCS sensors and actuators data architecture is described in Figure 4.1.

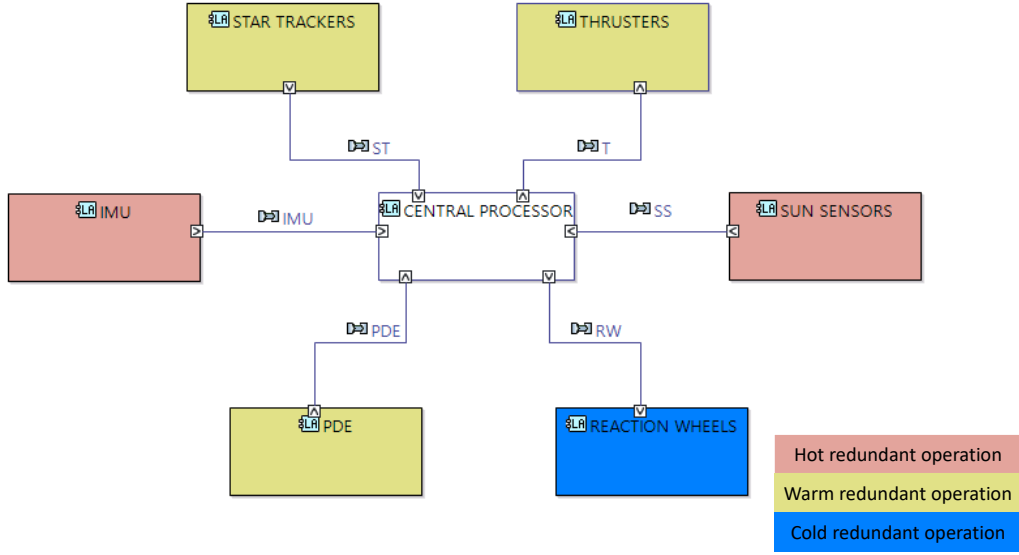


Figure 4.1: AOCS S/S architecture

As defined, on LRO three families of sensors and two families of actuators are mounted. These are installed in a redundant way to allow the orbiter to achieve mission goals even in presence of a non-critical component failure. The LRO relies on:

- **2 Star Trackers**, which provide the spacecraft attitude quaternion in the J2000 Earth Centered Inertial (ECI) reference frame. The choice of equipping the orbiter with 2 star trackers comes from accuracy and reliability requirements.
- **1 Miniature Inertial Measurement Unit (MIMU)**, which is a three-axis ring laser gyro able to provide accurate attitude rate information without using accelerometers.
- **10 Coarse Sun Sensors (CSS)** placed on the spacecraft in directions and locations which allow the Sun to be located when it is in view of any LRO surface. Design simplicity and lack of needed power are the reasons why these are the primary sensors used in Sun-Safe control mode [37].
- **4 Reaction Wheels (RW)**, specifically designed to provide smooth and quiet changes in spacecraft pointing attitude. Due to their working principle, reactions wheels need to undergo a momentum unloading manoeuvre (*Delta-H mode*) every 2 weeks in order to continue operations.
- **8 Thrusters** for orbit maintenance and attitude manoeuvres. These thrusters are monopropellant engines, mainly used in the Delta-H and Delta-V modes.

## 4.2 Mission Modes

To ensure requirements to be satisfied, LRO ACS operates four very distinct operating modes. Each of these uses a different set of sensors and actuators:

SENSORS and ACTUATORS	PERFORMANCES
Star Tracker [38]	20 arc-sec 90 arc-sec about boresight 16 deg field of view
MIMU [39]	0.2 arc-sec resolution, up to 375 deg/s 100 ppm linearity 5 ppm stability
Coarse Sun Sensor	170 deg field of view
Reaction Wheels	~90 Nms at 24V ~120 Nms at 31V >0.16 Nm torque
Propulsion Deployment Electronics	FPGA based electronics that control the thrusters, valves and deployment initiators. Provides safety inhibits.

Table 4.1: Sensor and actuator performances [4]

MODE	REQUIREMENTS
Observing	Pointing knowledge: less than 30 arc-sec Pointing accuracy: less than 45 arc-sec
Sun-Safe	The orbiter must be kept both thermally safe and power positive
Delta-H	Dump the orbiter's angular momentum
Delta-V	Change the orbiter's velocity for orbit control

Table 4.2: LRO mission modes [4]

**Observing Mode** Observing mode is LRO's primary attitude control mode, which provides full-sky 3-axis spacecraft attitude slewing and fine pointing for lunar nadir and off-nadir as well as inertial targets. This control mode is used for all nominal pointing and slewing operations including science data acquisition, instrument calibration, as well as initial attitude determination during **Delta-V** mode operation. The hardware used for this mode includes four reaction wheels RW, two star trackers, and one 3-axis inertial reference unit. Two quaternion output STs are operated continuously, providing a highly accurate attitude reference to ensure attitude performance during occasional single star tracker occultation. Attitude and rate sensor data is processed onboard using a six state Kalman filter, which estimates IRU (Honeywell's MIMU serves as a single IRU as it does not include 3-axis accelerometers to perform orbital determination) bias and spacecraft inertial attitude quaternions. The filtered quaternion data is used as the attitude source for onboard attitude control as well as the definitive spacecraft attitude for ground processing of science data. Control torque commands are generated using a standard PID type control law. This algorithm utilizes quaternion feedback proportionally-limited attitude error to ensure that all slews closely track the eigenaxis with a constant slew rate. An attitude limit is set to ensure ample torque margin at a slew rate of 0.1 deg/sec over the design system momentum range of 90 Nms. The observing mode controller is required to provide fine Nadir pointing with an absolute accuracy of 45 arc-sec, of which knowledge of 30 arc-sec measured relative to the prime ST reference and 15 arc-sec from the control algorithm. This allows to cope with the required pointing budget of 60 arc-sec. The kind of pointing to be performed is selected by ground operators. During lunar inertial pointing, reaction wheels keep the instruments boresight pointing continuously at the Moon surface, while solar arrays and HGA are respectively tracking the Sun and the Earth. In the Table 4.3 the LRO's instrument pointing budget is shown.

Instrument	LOLA	LROC NACs	CRaTER	LAMP	Mini-RF	Diviner	LEND	HGA	SA
AKE req. [asec]	206	206 - 1031	36000	216	2160	619	360	-	-
AKE Tot. [asec]	143	116 - 501	18898	215	2091	616	331	-	-
APE req. [asec]	3600	516 - 2063	126000	540	2160	1238	360	1080	18000
APE Tot. [asec]	158	131 - 516	18913	230	2106	631	346	1069	10097

Table 4.3: Instruments pointing budget [40]

**Sun-Safe Mode** The aim of this attitude mode is to point the spacecraft in a safe attitude so that it is both power positive and thermally safe. It is the mode in which the orbiter starts in and was used to

acquire the Sun after separation from the launch vehicle. Attitude information comes from MIMU and CSSs, while reaction wheels perform attitude changes. This mode comprehends a sub-mode, which is able to perform Sun pointing without the IMU in the event it is off or producing bad data by using the Sun sensors to derive rates. Sun-Safe mode can also be used in the event of anomalies detected on-board, such as a stuck solar array [4].

**Delta-H Mode** When reaction wheels reach *saturation*, this mode is activated. Reaction wheels are spun to a specific speed (momentum unloading), while LRO attitude 22 N thrusters are turned on in order to maintain a desired attitude all over the mode duration. This mode holds the commanded attitude by propagating rates measured by the IMU.

**Delta-V Mode** This mode holds the commanded attitude by propagating rates measured by MIMU while provides changes in the orbiter velocity (orbit adjustments and maintenance). The 90 N insertion thrusters are only used for the lunar orbit insertion maneuvers, and, in that configuration, the 22 N attitude control thrusters are on-pulsed for control. All other maneuvers only use the 22 N attitude control thrusters, operating in an off-pulse configuration. Mission trajectory and accumulation of external disturbances acting on the nominal orbit lead LRO to enter this mode.

Although the orbiter autonomously enters a lower-state control mode when an anomaly is detected, ground commands must be provided to move the spacecraft into a higher-state control mode. *Delta-V* mode can only be entered from Observing mode, while *Delta-H* mode can be entered from either sun safe or observing (Figure 4.2). The thrusters will return to the mode from which they were called after a normal or anomalous termination [4]. This control architecture combines the capability of precise pointing with on-demand repointing. It provides simplicity to the operation of the S/C while keeping it safe, as well as additional flexibility for science data collection.

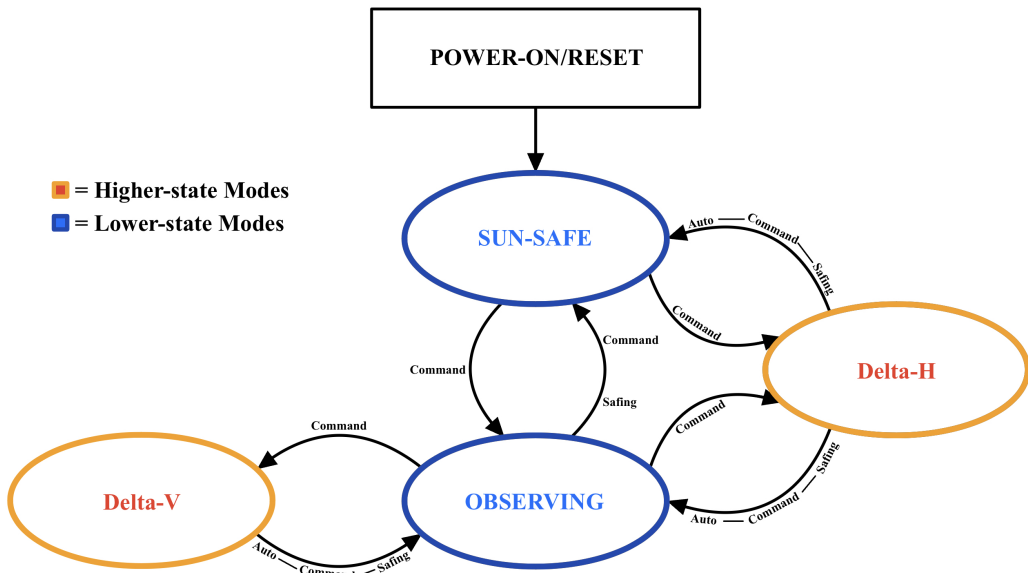


Figure 4.2: LRO mission modes [4]

#### 4.2.1 Commissioning phase

**Observing mode performance** LRO demonstrated excellent pointing performance during Observing mode nadir and inertial attitude target operations along the entire Commissioning phase. LRO pointing requirements are given as pointing accuracy and knowledge relative to the prime star tracker reference frame. However, there is no direct measure of pointing accuracy relative to this frame. Therefore, the derived attitude control error requirement of 15 arc-sec (3 sigma) was used to assess pointing performance. Transients LRO attitude errors observed during commissioning phase is derived from four sources: Diviner instrument calibrations, RW zero crossings, SA articulation and non-constant nadir target rate resulting from the low-lunar-elliptic commissioning orbit. Even during times of considerable disturbance, primarily due to RW zero crossings and SA articulation as shown in Figure 4.3b, the attitude errors were maintained below the statistical attitude error requirement level of 15 arc-sec.

**Diviner Instrument Calibration Disturbance** Figure 4.3a shows attitude error for a typical orbit during nadir target operations. Attitude errors remain below 2 arc-sec, with the exception of transients caused by Diviner instrument motion. There are two types of Diviner motion that caused spacecraft pointing error. The smaller disturbance was caused by a “barrel roll” or elevation-only gimbal motion for pointing the instrument to deep space for calibration. These occurred at 10 minute intervals and resulted in less than 5 arc-sec pointing error, primarily about the spacecraft roll axis. The error in the yaw axis is a result of two axes motion of the Diviner azimuth and elevation gimbals occurring once per orbit.

**RWs Zero Crossing and SA harmonic Disturbances** The pointing error increase when the SA is tracking the Sun and the RWs are crossing zero speeds. The worst case transients cause pointing error of  $\sim 50$  arc-sec as shown in Figure 4.3b. As X-Z momentum increased at higher rates than pitch axis momentum wheel speed zero crossings continued to occur at each orbit. During subsequent Delta-H wheel momentum unloading, pitch momentum biasing was used to minimize low speed wheel operation while maintaining system momentum within 80 Nms over a required two week period. Although using this strategy, it was not always possible to entirely avoid zero crossings within the system momentum constraints.

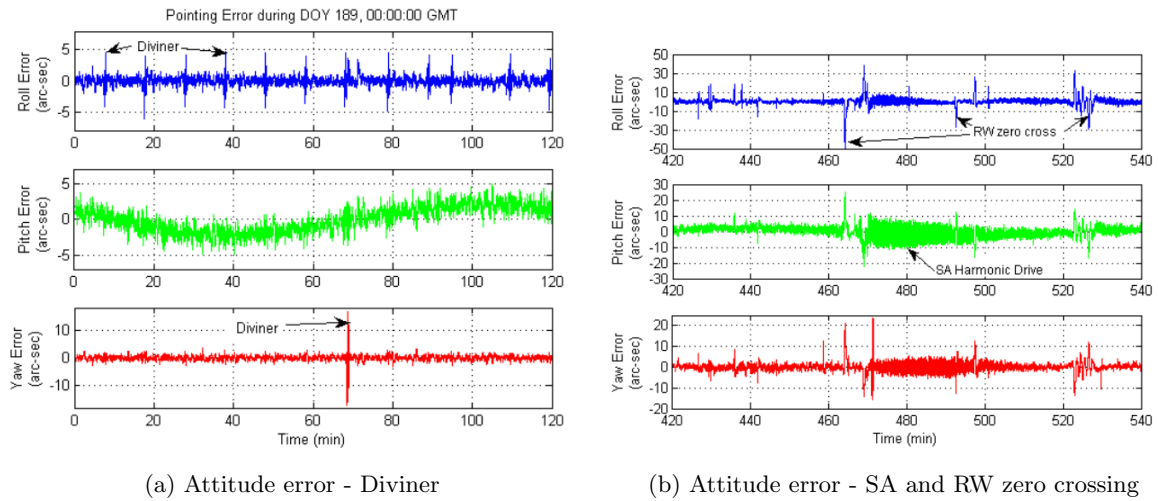


Figure 4.3: Attitude error disturbances [41]

### 4.3 Sizing & Configuration of the AOCS

The positioning of each elements in the spacecraft’s design shall consider the behaviour of Inertia Moments and the position of the CM to obtain an higher stability. The CAD model is a rough approximation of the real model, which considers the PS, SA, HGA and the scientific payload. Each element with their corresponding dimensions and masses is taken into account. For simplicity, as shown in Figure 4.4 the cables and heaters are not considered, therefore the final values, in terms of inertia moments and masses, may differ from the real case.

The origin of the reference system used from here on is located as follows:

- $+x$  axis: located along the symmetry axis of the tanks. It is also the direction of the orbital velocity.
- $+y$  axis: located on the plane of the thruster support structure (represented in green color in Figure 4.4). It is also the out-of-plane vector of the orbit.
- $+z$  axis: it completes the right-handed orthogonal reference system. It also is the direction along which the instruments perform observations, and points directly towards the surface of the moon during nominal operations.

### 4.4 Sensor Selection & Actuator Sizing

In this section the selection and sizing of sensors and actuators is performed. The ACS instruments suite can be understood by looking at the mission requirements and disturbances acting on the orbiter

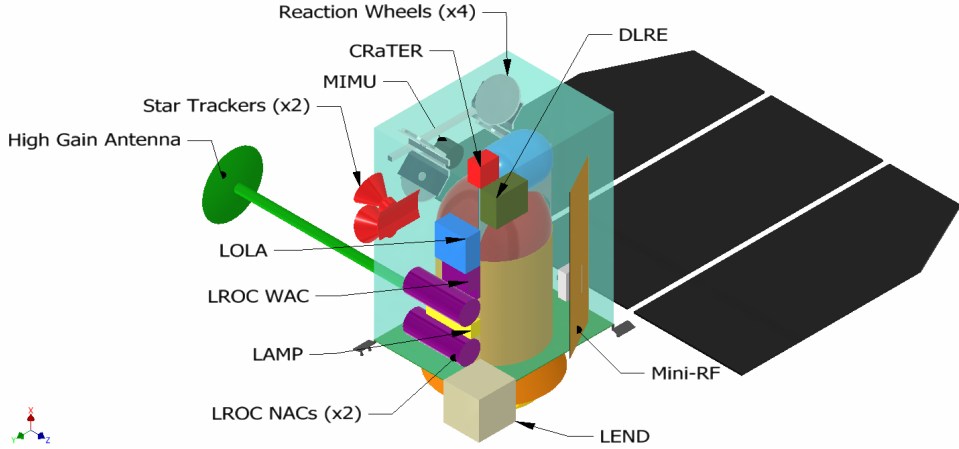


Figure 4.4: CAD model with the onboard instruments

SENSORS & ACTUATORS CONFIGURATION	
<b>Position of the CM [mm]</b>	<b>Full</b>
<i>x</i>	654.731
<i>y</i>	19.028
<i>z</i>	-48.736
<b>Mass moment [kgm<sup>2</sup>]</b>	
<i>I<sub>xx</sub></i>	741.251
<i>I<sub>xy</sub></i>	-46.104
<i>I<sub>xz</sub></i>	-14.863
<i>I<sub>yy</sub></i>	1191.883
<i>I<sub>yz</sub></i>	-13.356
<i>I<sub>zz</sub></i>	1157.928

Table 4.4: LRO inertia properties derived from sensors and actuators configuration

during its lifetime. The nature of the scientific observations to be performed on the lunar surface, and the fact that they involve mapping the surface itself, leads to high-accuracy requirements for both attitude determination and control, as discussed in Section 4.2.

#### 4.4.1 Disturbances

As a first approximation, the GG and SRP disturbances are considered. Tables 4.5a and 4.5b show the parameters used for the computation of the worst-case disturbance torques. It is worth noting that neither drag nor magnetic disturbances are considered. This is due to the extremely low pressure and density of the Moon atmosphere [42], and the extremely low intensity of the lunar magnetic field in comparison with that of the Earth [43] [44].

To consider the worst case scenario, the nominal orbit with 50 km of altitude is analyzed. The maximum deviation of z-axis from the local vertical is defined equal to 45 deg, while the maximum and minimum inertia axis are taken from the CAD model.

Gravity Gradient	Value
$\mu$ [km <sup>3</sup> /s]	4030
$R_{min}$ [km]	$R_{moon} + 50$
$I_{max}$ [kgm <sup>2</sup> ]	$I_{yy}$
$I_{min}$ [kgm <sup>2</sup> ]	$I_{xx}$
$\theta_{GG}$ [deg]	45
Torque [Nm]	<b>5.09 · 10<sup>-4</sup></b>

(a) GG torque evaluation

SRP	Value
$F_s$ [W/m <sup>2</sup> ]	1367
$A_s$ [m <sup>2</sup> ]	13.6567
$q$	0.3
$C_{SP}$ [mm]	[126 ; -2565 ; 0]
Torque [Nm]	<b>2.13 · 10<sup>-4</sup></b>

(b) SRP torque evaluation

Table 4.5: Attitude disturbances evaluation

As an approximation for the calculation of the SRP torque, only the SA area is considered: the effects of the SRP on the spacecraft body are neglected due to its quasi-symmetrical geometry. The SA area and the

distance of the  $C_{SP}$  to the CM are considered with margins in order to perform a conservative estimation of the disturbance torque. Furthermore, the CM is shifted with respect to the position retrieved from the CAD due to the presence of an uncertainty on the location of the CM, as seen in Table 4.6. Moreover, the CM changes position due to factors such as moving components and fuel consumption. For simplicity, the position of the centre of SRP is fixed in the geometrical center of the SA.

In terms of magnitude, both the GG and SRP torques are comparable. As mentioned before, the internal disturbances must also be taken into account. Transient LRO attitude errors observed during the commissioning phase resulted primarily from three sources: DLRE instrument calibrations, RW zero crossings, and SA articulation. Even during times of considerable disturbance from SA articulation, the attitude errors were maintained below the statistical requirement level of 15 arc-sec [45]. Due to structural-dependent behaviour and low amplitude, the dynamics of moving appendices was not considered in the global computation.

The perturbations that bring uncertainty to the system are shown in Table 4.6.

DISTURBANCE	EFFECTS	CONSIDERED VALUES
Uncertainty of the CM location	Unbalanced and unwanted torques	$\pm 15$ [mm]
Thruster Misalignment	Unbalanced and unwanted torques	0.3 [deg]
Mismatch of Thrusters Outputs	Unbalanced and unwanted torques	$\pm 5$ %

Table 4.6: Internal disturbance sources

#### 4.4.2 Sensor selection

As previously mentioned, the nature of the scientific mission lead to the accuracy requirements of the sensors. By correlating the specified attitude determination requirement for each mode [37] with the utilized sensors on the market (their performances are shown in Table 4.1, the selection of the sensors can be performed, as seen in Figure 4.5.

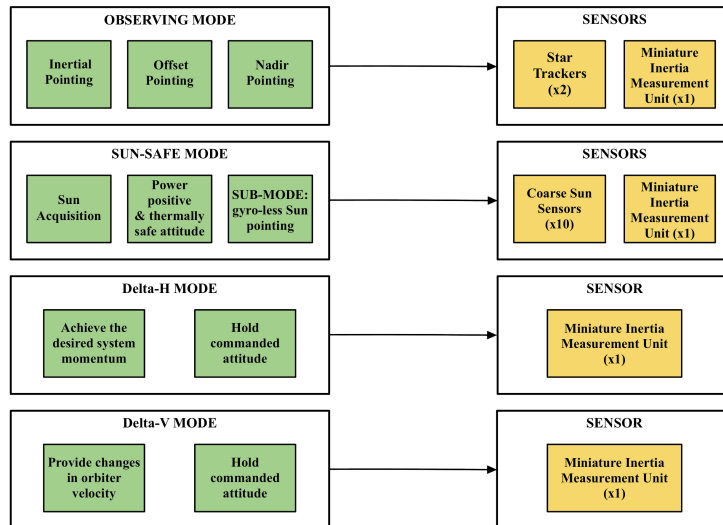


Figure 4.5: Sensor selection rationale

#### 4.4.3 Actuator selection

The RW sizing process was performed in two steps: firstly, the computation of the required torque and, secondly, the momentum storage needed (both in the BARF). As mentioned in Subsection 4.4.1, only the GG and SRP torques are considered. The computation of  $T_{RW,yaw}$  was done by considering a 180 deg yaw manoeuvre performed with a slew rate of 0.1 deg/s [46] (this is extremely conservative because the orbiter actually performs a 180 deg manoeuvre over one full orbit). Another slew manoeuvre is also taken in account. For this general case, the slew rate is fixed to 0.5 deg/s; with this assumption the worst case scenario is modelled. The actual required  $T_{RW}$  is the sum of the torque needed to compensate the

disturbances and the one required to complete the slew manoeuvre in the specified time. It is important to note that the value of  $T_{RW,disturbances}$  is given in the BARF, so the actual  $T_{RW}$  must be computed taking into account the configuration matrix of the pyramidal layout of the RWs [47]. From the calculated angular momentum stored during one orbital period,  $h_{RW,required}$ , and the actual capacity,  $h_{RW,capacity}$  (given in the BARF), the number of orbits between desaturation manoeuvres is calculated, which gives the time between Delta-H mode entries. All of the aforementioned values are reported in Table 4.7a.

RW Data	Value	Margins
$T_{RW,disturbances}$ [Nm]	0.001464	100%
<b>Slew manoeuvre</b>		
$T_{RW,slew}$ [Nm]	0.1156	-
$\theta_{slew}$ [deg]	180	-
$t_{slew}$ [s]	360	-
<b>Yaw manoeuvre</b>		
$T_{RW,yaw}$ [Nm]	0.0046	-
$\theta_{yaw}$ [deg]	180	-
$t_{yaw}$ [s]	1800	-
<b>Momentum storage</b>		
$h_{RW,required}$ [Nms]	1.7555	-
$h_{RW,capacity}$ [Nms]	92.376	-
$N_{orbits,desaturation}$	105.24	-
$T_{desaturation}$ [days]	8.2639	-

Thrusters Data	Value	Margins
$F_{th}$ [N]	$7.96 \cdot 10^{-4}$	-
<b>Propellant related</b>		
$t_{burn}$ [s]	9.6783	100% <sup>1</sup>
$t_{burn,tot}$ [s]	861.3673	-
$I_{SP}$ [s]	228	-
$N_{burns}$ [-]	89	-
$M_{desat}$ [kg]	8.4724	-
$M_{SK}$ [kg]	91.5	Deterministic [4]

(a) ACS RW sizing

(b) AOCS thrusters sizing

Table 4.7: Actuators sizing results

The physical configuration of the thrusters was considered during the sizing process, along with the uncertainties related to the manufacturing tolerances of the manifolds, thrust chambers, nozzles and the potential misalignment of the actuators. The values reported in Table 4.7b refer to the sizing of the thrusters regarding the RW desaturation. The burn time reported in Table 4.7b references the impulse required to go from a "very positive" to a "very negative" condition of the RW's angular momentum [37], which effectively means that the required impulse is doubled <sup>1</sup>. The required thrust level was calculated, along with the torque contributions along the body axes, by considering the 3D configuration from the CAD model, and is several orders of magnitude lower than the actual value, which is due to the usage of the ACS thrusters for the SK manoeuvres.  $M_{desat}$  was computed considering the calculated number of burns for a two-year span, along with the burn length as previously mentioned.  $M_{SK}$  was taken from Reference [4] because calculating it would require an in-depth analysis of the orbital mechanics regarding the nominal orbit and its disturbances.

## 4.5 Power & Mass Budget

In Table 4.8, the power consumption and masses of each element of AOCS subsystem are listed. The RWs have a higher power consumption because they are tasked with ensuring the correct attitude of the S/C. Both RWs and PDE have larger masses with respect to other AOCS components, which is why they are fixed in opposite sides of the S/C configuration, for stability reasons [4].

AOCS component	Power [W]	Mass [kg]	Qty.
<b>Star Tracker</b>	11.2	4.2	2
<b>MIMU</b>	25	4.5	1
<b>CSS</b>	0	0.0011	10
<b>RW</b>	16.6	11.9	4
<b>PDE</b>	13.2	9.4	1
<b>Total</b>	<b>127</b>	<b>70.01</b>	-

Table 4.8: AOCS power and mass budget

<sup>1</sup> Going from the maximum positive  $\omega$  of the RWs to the maximum negative  $\omega$  yields a change in angular momentum equal to two times the storage capacity, which is why the margin is considered.

## Chapter 5

# Thermal Control Subsystem

### Change log

- **Sec. 5.1** pp 34: Table 5.2 OSR BOL emissivity value added; Temperature margin justification
- **Sec. 5.3.2** pp 36, 37: Figure 5.2 change for better interpretation and comment to the graph. Table 5.7 added S/C column for mononode analysis, comment on mononode heaters.
- **Sec. 5.3.3** pp 37, 38: Introduction change. MLI and aluminum parameters added. Comment on radiator size.

The LRO TCS shall provide protection from the lunar thermal environment that is one of the harshest in the solar system due to lack of the atmosphere, low effective regolith conduction and high infrared loading caused by low albedo [48].

## 5.1 TCS Architecture

Being the mission schedule requirement one of the main driver of the project, the TCS design is carried out in order to have a fast I&T (Integration and Test) phase, which is demanded from an economic and time view point. To fulfill this condition, the design process shall comply with the following guidelines as much as possible [48]:

- **Modular design:** this project philosophy allow the hardware to be built and tested in parallel, splitting the building location and technicians' work.
- **Simplicity:** number of radiators, thermal interfaces and blankets shall be minimize. Moreover, components with similar thermal requirements shall be linked together.
- **Unfilled space:** the thermal design shall not rely on empty space of the mechanical model because it is not fixed until the CDR (*Critical Design Review*) phase.

Furthermore, in order to allow the survivability of the S/C, the redundancy of the critical heaters and heat pipes has been designed. Optimal point direction and clear radiators FOV shall be ensured [48].

The *modular design* philosophy is the most evident characteristic of this subsystem. It is divided in four independent modules.

**Avionics module** The avionics module is characterised by two main parts (Figure 5.1): an aluminum honeycomb panel on which avionics components (Y face) are placed and avionics thermal radiators placed on -Z face (zenith direction). Most of the structure, in particular avionics instruments, batteries and RWs, is thermally coupled to the radiator by aluminum-ammonia HP. These components represent a large thermal inertia which reduce the sensitivity to the temperature variation (i.e. over the lunar eclipses period).

On the other hand, the majority of the scientific instruments are thermally insulated from the structure (Table 5.1) therefore they have their own radiators and heaters. The main radiator is covered with Optical Surface Reflector (OSR), which allows to reflect most of the incoming energy from the Sun and emit in the IR.

The heat pipe network in this module is divided in two main parts; in the avionics panel are embedded CCHP (Constant Conductance Heat Pipe), while the link between the panel and the radiator is established by VCHP (Variable Conductance Heat Pipe) which allows to control the heat flux driven to radiator [40].

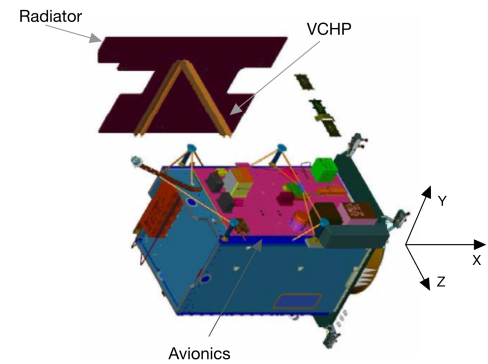


Figure 5.1: Avionics module configuration

Instrument	CRaTER	Diviner	LAMP	LEND	LOLA	LROC	Mini-RF
Thermally coupled	X			X			X
Thermally isolated		X	X		X	X	

Table 5.1: Instruments thermal coupling [40]

**Instrument bench module** The instrument bench accommodate the instruments that require an accurate pointing: LOLA, LROC, LAMP, and the Star Trackers. It is mounted on the opposite face of the *avionics module* (Y face) to improve the mass balance [4, 48]. The bench structure is realized in M55J, high modulus carbon fiber, which is characterized by high stiffness that fulfills the instrument pointing requirements, but has a lower thermal conductivity with respect to aluminum that composes the main structure. In order to maintain the module temperature in the desired range, 25 small operational heaters are mounted on the module [48]. The installed heaters are small in order to reduce the thermal gradient in the low thermal conductivity bench. Differently from the *avionics module*, each instrument has its own radiators. A clear FOV shall be granted for each instrument radiator.

**HGA & SA System module** The critical point of the HGA system from a thermal and mechanical view point is the gimbal system. The TCS shall be able to manage the dissipated power between the amplifier and the antenna's dish ( $\sim 20\text{ W}$ ). The HGA system can not be thermally coupled to other parts of the spacecraft bus because of the rotational joints. Therefore, multiple radiators and heaters have been installed in this region. Around 40 separated blankets have been used to manage its heat flux [48].

In the SA system, the hot surface of the solar panels shall be thermally insulated from the dual-axis gimbal system [48]. In order to keep the actuators and dumpers in the operative temperature range MLI, dedicated radiators and heaters have been exploited [4].

**Propulsion module** The TCS shall maintain the correct temperature of the propellant inside the tanks. The allowable temperature range of the Hydrazine storage is between  $+15$  and  $+50\text{ }^{\circ}\text{C}$  [49]. In order to achieve this requirement the two upper and lower hydrazine tanks are thermally coupled to a central cylinder covered with heaters. All the propulsion system is radiatively isolated from the S/C with blankets and a VDA double layer film [48].

**Multi Layer Insulation and OSR** The majority of the S/C external surface is covered by 3 mil MLI composed by an average of 15 layers<sup>1</sup>, which insulate the satellite from the external environment. In Table 5.2 the MLI characteristics are reported.

The OSR (covering the main thermal radiator) optical properties<sup>2</sup> and characteristics are reported in Table 5.2. The OSR EOL value is obtained considering an increase of 250% according to typical literature aging [18].

Material	Application	$\alpha$	$\epsilon$
VDA	MLI inner layers (14)	0.08 (0.1)	0.05 (0.03)
Germanium-coated Kapton	MLI outer layer	0.49 (0.51)	0.81 (0.78)
OSR with Iridium Tin Oxide coating	Radiator	0.063 (0.16)	0.8 (0.785)

Table 5.2: Materials optical properties BOL (EOL)

**Temperature limits** The TCS shall ensure the correct thermal environment for all the component of the S/C. In Table 5.3 the temperature ranges of the main components of the S/C are reported; the data are taken from [40] PDR (*Preliminary Design Review*) document related to phase B, therefore a  $\pm 10\text{ }^{\circ}\text{C}$  margin on the temperature limits is adopted [18]. From these temperature limits a global range has been adopted applying  $10\text{ }^{\circ}\text{C}$  as margin. As a result, the global temperature limits become  $T_{min} = 10\text{ }^{\circ}\text{C}$  and  $T_{max} = 20\text{ }^{\circ}\text{C}$ . Components as CRaTER, batteries and Hydrazine tanks are at the interval limits, therefore an independent temperature regulation is required.

Instrument	$T_{min}$ [ $^{\circ}\text{C}$ ]	$T_{max}$ [ $^{\circ}\text{C}$ ]	Component	$T_{min}$ [ $^{\circ}\text{C}$ ]	$T_{max}$ [ $^{\circ}\text{C}$ ]
CRaTER	-30	25	Batteries	10	30
DRLE	-20	45	Hydrazine Tanks	10	40
LAMP	-30	30	Star trakers	-30	50
LEND	-20	40	RWs	0	50
LOLA	-30	30	SA	-125	135
LROC	-30	30	HGA	-140	145
Mini-RF	-30	50	Omni	-120	80
			C&DH	-10	40

Table 5.3: Temperature limits of payload instruments and components [40]

## 5.2 LRO Thermal Environment

The LRO goes through different operative conditions from separation to mission orbit operations. In order to properly size the TCS the most extreme scenarios shall be identified. The hot and cold scenarios

<sup>1</sup>The number of layer varies with the position on the S/C

<sup>2</sup>The optical properties reported are not the specific but typical

are given both by external environment contribution, depending on S/C orientation, and on internal power dissipation.

- **Early phases:** The main thermal flux contribution is the Sun. The contributions from Earth IR emission and reflection are also present. In these phases the attitude is not constrained, therefore the components temperature can be managed changing the S/C orientation [40]. Low internal power dissipation, neither instruments, nor communication devices are active [50].
- **Lunar transfer & LOI:** The only heat source is the solar radiation for the most part of this phase. During LOI a secondary contribution is given by Lunar reflection and IR emission. The internal heating increases due to the beginning of communications [50].
- **Commissioning orbit & Measurement operations:** Due to the lack of atmosphere and the slow rotation, the lunar surface temperature can range from 84 K to 391 K [51], according to the exposure to sunlight. This leads to high infrared loading from the surface directly illuminated by the Sun. During this two phases LRO might experience both extreme conditions due to the variation in  $\beta$  angle: At the sub-solar point the external thermal fluxes are maximum and the zenith facing radiator is hit by the solar radiation; at  $\beta = 90^\circ$  the heat fluxes from the moon are reduced and the radiator faces only the deep space therefore the sun radiation, arriving on the MLI cover, is almost totally insulated [4]. All the instruments and the remaining S/C subsystems are activated, the internal power is at its maximum [50].
- **Eclipse phases:** The only contribution comes from the IR emission of the lunar surface at very low temperatures. During the measurement operations eclipse occurs for orbit with  $\beta$  between  $76.4^\circ$  and  $0^\circ$ , the longest eclipses last 48 minutes at  $\beta = 0^\circ$  [40]. Moreover the Moon can cross Earth shadow, the most severe event is the total lunar eclipse expected in June 2011 [48]. During these passes the S/C is pre-heated to minimize the heaters power required [4]. The S/C enters the Safe hold mode, the instruments are switched off and no communication occurs. The generated thermal power is at its minimum since the Commissioning phase [50].

## 5.3 TCS Sizing

In order to validate the retrieved data on LRO TCS a thermal analysis is conducted.

### 5.3.1 Preliminary Study

The whole spacecraft is modelled as a single sphere of equivalent area, the real dimensions and the sphere radius are reported in Table 5.4. The solar panel, being independent from the primary body, is completely excluded from the study.

$L_x$	$L_y$	$L_z$	$r_{sphere}$
2.7 m	2 m	1.4 m	1.38 m

Table 5.4: S/C dimensions [52]

Before executing the first analysis, a preliminary study on the possible scenarios shall be performed. To obtain the sizing condition, the hotter and the colder cases shall be detected.

Based on the MA section the cases considered are:

- **Hot scenarios**
  - Sub-solar point of the commissioning orbit, with a true anomaly equal to  $90^\circ$  and a beta angle equal to zero (H1).
  - Sub-solar point of the operational orbit, with an average altitude equal to 50 km (H2).
- **Cold scenarios**
  - Apocentre of the commissioning orbit. It is the farther point from the moon at altitude 216 km (C1).
  - Operational orbit with a beta angle equal to  $90^\circ$  where the Infrared Moon flux is low (C2).
- **Non-nominal scenarios**

- Deployment condition, after the separation of the spacecraft from Centaur. In this phase the infrared flux of the Earth is screen by the atmosphere and the heat generated internally is very low (NN1).
- Moon transfer orbit. At 200000 km from Earth the temperature are very low due to the heat flux encountered. However in this phase the instrument onboard are not operative, and therefore there are no strong attitude constraints to be respected. According to [40] the satellite is shifted in survival mode. For all these reason this case is analyzed but is not taken into account for sizing (NN2).
- The eclipse conditions on the operational orbit. In this scenario the S/C operates in survival mode and it also is characterized by a non-steady-state thermal condition therefore this case is not taken into account for sizing (NN3).

The values adopted for the computation of the different scenarios are reported in Table 5.5. The maximum and minimum solar flux varies based on the distance between the sun and the Moon. The variability of the albedo factor is related to the angle of the reflected radiation.

The view factor for a small sphere with respect to the moon varies with the orbit altitude [36]:

$$F_{sp} = \frac{1}{2} \cdot \left[ 1 - \frac{\sqrt{\left(\frac{\text{altitude}}{R_{\text{moon}}}\right)^2 + 2 \cdot \frac{\text{altitude}}{R_{\text{moon}}}}}{\frac{\text{altitude}}{R_{\text{moon}}}} \right]$$

Scenario	$\dot{q}_{\text{Sun}} [\text{W}/\text{m}^2]$	$\dot{q}_{IR} [\text{W}/\text{m}^2]$	Albedo Factor [-]
<b>Hot case</b>	1420	1340	0.13
<b>Cold case</b>	1280	5	0.06

Table 5.5: Heat fluxes in hot and cold scenario [4]

The considered internal power generation is taken from [50], assuming a margin of 30% to be conservative. The results of the preliminary analysis are shown in Table 5.6, the heat fluxes are computed assuming unitary emissivity and absorptance.

For the sizing, the hot case scenario considered is the operational orbit at sub-solar point. On the other hand the C1 and C2 scenarios are similar. Reducing the optical properties the internal power dissipation became slightly more relevant and the  $\dot{Q}_{tot}$  may change, therefore C1 may became hotter than C2. Considering some margin in the heater power supplied both cases can be respected. As a result the selected cold scenario is C2.

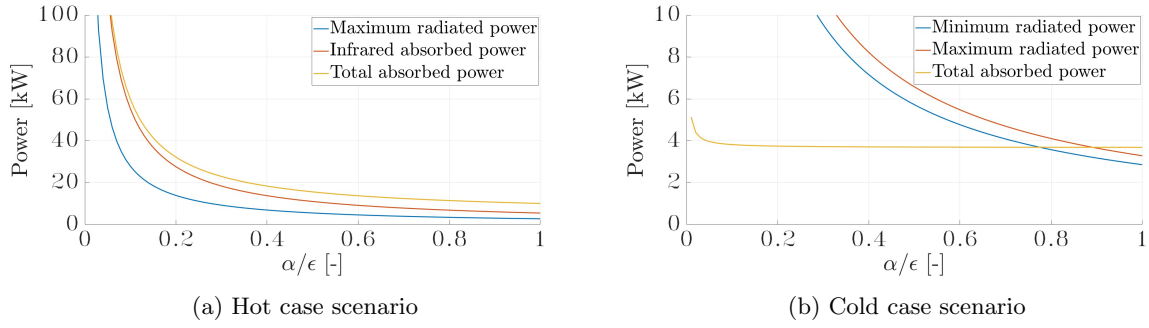
Heat Fluxes	H1	H2	C1	C2	NN1	NN2	NN3
$\dot{Q}_{int} [\text{W}]$	671.79	604.19	671.79	604.19	269.36	393.20	312.60
$\dot{Q}_{tot} [\text{kW}]$	21.0	23.1	8.87	9.02	12.5	8.06	0.358

Table 5.6: Internal dissipated power and total power absorbed in the analyzed scenarios

### 5.3.2 Single-Node Analysis

For the two extreme conditions previously identified a single node analysis is performed. The S/C is approximated as a homogeneous sphere, with constant optical properties all over the surface. The node temperature shall be in the range identified by the components operational ranges, considering the maximum of the minimum temperatures and the minimum of the maximum ones. The components that are at the limits (Table 5.3) shall be individually controlled, such as CRaTER, whose maximum temperature is limited at 25°C.

A value of  $\alpha/\epsilon$  ratio that allows the S/C to operate inside the fixed temperature interval is searched. The values adopted in the modelling of the cold and hot scenarios are reported in Table 5.5. In Figure 5.2 the analysis for the single-node S/C is reported. The absorptance in the IR spectrum is assumed equal to the emissivity, according to Kirchhoff's law. As a result in the hot case the infrared flux from the Moon is larger than the power that can be radiated towards deep space for every emissivity value. The maximum temperature cannot be granted in steady state for the mononode analysis. An additional radiator is needed, in order to increase the radiated power while reducing the absorbed one. In the cold case scenario the equilibrium can be reached for a value of  $\alpha/\epsilon$  ratio between 0.78 and 0.90. For larger  $\alpha/\epsilon$  the S/C temperature increases above the maximum temperature while for smaller  $\alpha/\epsilon$  values the



(a) Hot case scenario

(b) Cold case scenario

Figure 5.2: Absorbed and radiated power in hot and cold scenarios

S/C temperature is below the minimum and the addition of heaters shall be taken into account. In order to keep the S/C inside the desired temperature range a complete insulation is needed. The S/C must be separated from the external heat sources and only the internal power shall be dissipated to outer space through a radiator. All the avionics component and the coupled instruments (Table 5.1) are included in the internal power dissipation. Using an OSR radiator, with emissivity value of 0.785, the radiator surface is computed. This process is repeated for the thermally decoupled instruments, considering only their internal power. Results are reported in Table 5.7.

Instrument	S/C	LROC	LAMP	LOLA	Diviner
$\dot{Q}_{int} [W]$	521.6	28.6	5.59	34.1	14.3
$T_{desired} [^{\circ}C]$	20	5	20	20	25
$A_{radiator} [m^2]$	1.58	0.107	0.017	0.104	0.041

Table 5.7: Mononode results [53]

The radiator surface is computed considering the maximum internal power. Whenever the internal power is lower the S/C temperature decreases. To keep the S/C temperature inside the range the dissipated power shall be at least 454 W, therefore during the non nominal phases (Table 5.6) the heaters shall be switched on generating at most 185 W of thermal power. A similar conclusion can be derived for the insulated instruments: whenever not operative an heater shall be switched on.

### 5.3.3 Multi-Node Analysis

A more in dept analysis is performed for the S/C considering a non perfect insulation from the external environment and adopting the correct attitude. A Kapton-VDA MLI is installed on all the S/C surfaces except for the OSR radiators. The MLI is modelled according to [36], granting a total emissivity value of 0.001, assuming 15 layers in materials EOL conditions. The hot scenario will be treated at first in order to properly size the radiator area.

A Multi-Node study is performed. On the S/C, three nodes have been selected:

- External layer of the MLI. The internal surfaces are made of VDA while the external surface is Germanium coated Kapton (Optical properties in Table 5.2).
- Aluminium case of the S/C characterized by low emissivity (0.15 [50]). It represents all the primary structure and its content and all the instruments that have no specific thermal control.
- Main radiator in OSR (Optical properties in Table 5.2).

The external sources considered are the Deep Space, the Sun and the Moon.

The interaction between the nodes is modelled exploiting thermal resistance (Figure 5.3). Table 5.2 shows the optical properties adopted.

According to [4] the zenith-facing radiator is thermally coupled through a HP network with most of the structure to provide thermal dumping. Therefore the thermal resistance between the radiator and the main body is modelled with a fictitious aluminium alloy heat pipe (6061-T651) with conductivity 167 W/mK [54]. The contact area is assumed as 5% of the whole radiator surface, while the HP thickness is assumed equal to 1 mm. The radiative resistance between the two nodes is considered negligible.

The internal heat flux accounts for the coupled components. It is located in the S/C case node and it is equal to 521.6 W [50], considering a margin of 30%.

The view factor for the IR and albedo flux considered the S/C as a sphere of area equal to the total area

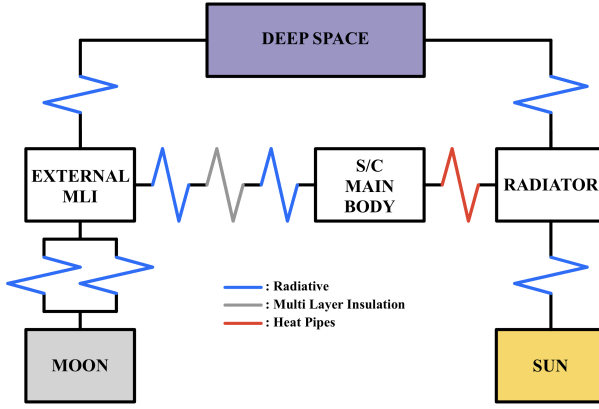


Figure 5.3: Thermal resistance scheme for the hot scenario

(included the radiator area). For the calculation of the Sun heat flux, the illuminated face is known from the attitude and therefore the specific rectangular area is considered: the radiator area in the hot case, the +X axis S/C surface in the cold case.

Exploiting the model just described, the desired temperature of the aluminium case is fixed to the maximum possible value and the requested radiator area is obtained. For the cold case scenario, the radiator area is now fixed. The attitude is different because the Sun radiation hits the MLI surface and the radiator is only dissipating towards the DS. The internal desired temperature (of the S/C main body node) is fixed to the minimum possible value. The model output is the requested heaters power. Results are shown in Table 5.8.

Node	$A [m^2]$	$T_{HOT} [^\circ C]$	$T_{COLD} [^\circ C]$	$\dot{Q}_{heaters} [W]$
MLI	18.63	124.07	-3.20	-
Case	18.63	20.00	10.00	1003
Radiator	5.33	19.99	9.98	-

Table 5.8: Multi-nodal analysis results

According to literature [4], the radiator area covers most of the -Z S/C surface, therefore the results obtained are compatible. **The large increase in radiator surface with respect to the mono-node analysis is mostly related to the S/C attitude considered limiting the insulation from the external heat sources.** Moreover the temperature obtained on the MLI node respects the admissible limit [55]. In the cold case, the maximum available power of 1317 W [40] can be exploited for the S/C survivability during the eclipses. In this report the transient conditions are not analyzed, but the obtained results shall be validated also for the eclipse phase. In a single-node approach the stringent temperature of a specific element affect the temperature of the whole node and therefore the radiator sizing. For an advanced design the local temperature effect shall be taken into account and therefore final values may be different. Moreover, the optical properties of the MLI depends on specific point on the S/C because different part are covered with a different number of layers. The entire study is based on the steady state condition, which is a strong assumption with respect to the extremely variable environment the S/C goes through. The radiative exchange between the S/C and the solar panel is completely neglected in this report.

### 5.3.4 Mass, Power & Data budgets

The TCS mass budget data are reported in Table 5.9.

Component	Sensors	Heaters	Hardware	MLI	Total
Mass [kg]	2.4	0.4	5.2	18.9	<b>26.8</b>

Table 5.9: TCS mass budget [40]

The TCS power budget is mostly related to the heaters dissipated power. It varies according to the mission phase up to a maximum of 1317 W during Safehold mode at  $\beta = 90^\circ$  [40].

The installed sensors (Thermistors YSI 2.252  $k\Omega$  [40]) have a precision of 0.05  $^\circ C$  [56], the required number of bits is 5, therefore 8 bits are needed.

# Chapter 6

## Electric and Power subsystem

### Change log

- **Sec 6.1** pp 40: General consideration on SA solution.
- **Sec 6.1.1** pp 40: SA configuration and modules.
- **Sec 6.1.2** pp 40,41: Regulation and bus voltage, PSE consumption, PSE modules.
- **Sec 6.1.3** pp 41: Battery DOD in different phases, battery configuration.
- **Sec 6.3.1** pp 42,43: Detailed solar array sizing steps, real solar array comparison.
- **Sec 6.3.2** pp 43,44: Detailed battery sizing steps, real battery comparison.

## 6.1 EPS Architecture

The EPS is designed to receive energy from the Sun, convert it into electrical power, store (if needed) and deliver it to LRO during each phase of the mission (see Figure 6.1). To achieve this, a Direct-Energy-Transfer (DET) architecture is employed: this has a good efficiency level and is more suitable for mid/long term missions. It consists of three sub-elements: the SA, Power Subsystem Electronics (PSE), and the Battery [4]. SA are selected as primary energy source granting low mass and high efficiency in power production at 1 AU. RTGs would be more massive and require more thermal control effort. The aluminum primary bus structure and the propulsion module are electrically coupled to create a common grounding [40]. All S/C components shall be connected to the main structure with conductive elements or designated grounding points, using ground straps, in order to avoid undesired currents and discharges [40].

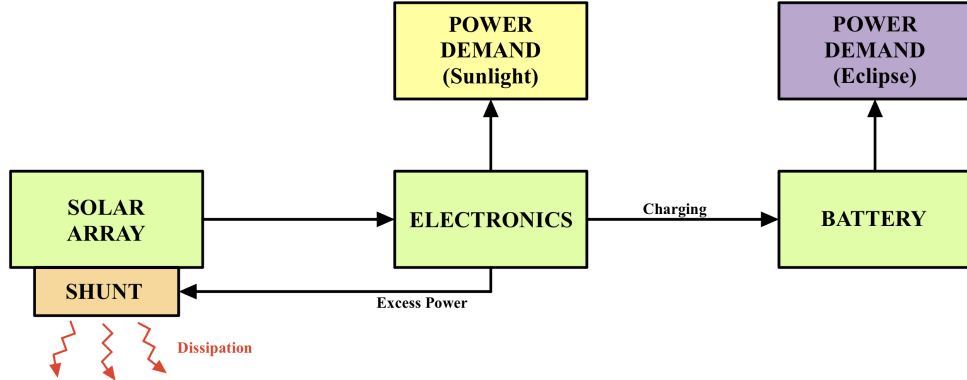


Figure 6.1: EPS architecture

### 6.1.1 Solar Array

The SA is used to convert sunlight energy into electrical energy while panels are in view of the Sun. The array configuration consists of Gallium Arsenide (GaAs) triple junction solar cells which are mounted on three aluminum honeycomb panels with composite frame. The two deployable lateral frames are connected to the central one through two hinges and present only 25 modules of cells (with respect to the 27 in the central panel). each module comprises 48 cells in 24 elemets series. These are continuously gimbaled in two axes to track the Sun [40]. The SA positioning shall not interfere with LROC FOV, reason why only 25 modules are installed on the side panels [40]. During sunlight operations, any excess power from the SA not needed for battery charging or spacecraft loads is rerouted back to the SA where a shunt allows for dissipation, as shown in Figure 6.1. The SA degradation characteristics are shown in Table 6.1, along with the value of solar irradiance, which corresponds to a distance from the sun of 1.0146 AU [4].

SOLAR ARRAY - PARAMETERS	VALUE
$\varepsilon_{BOL}$	0.3
$I_d$	0.77
$dpy$ [1/year]	0.0375
$I_0$ [ $W/m^2$ ]	1330

Table 6.1: Solar Array degradation parameters [18]

### 6.1.2 Power Subsystem Electronics

The basic design and operation of the LRO PSE is modeled after the architecture used on the Microwave Anisotropy Probe (MAP). LRO's PSE performs the functions of power distribution and battery charging using the SA. The electrical power is then transferred to the PSE, where it is conditioned and directed to all of the electrical loads connected to the spacecraft's unregulated bus, which operates between 22 and 35 V [40, 35]. This interval allows instruments operations within a safe range, accounting for line losses. Some instruments shall operate only above 27 V therefore they are switched off in case of low tension to avoid malfunctioning. Power control is performed using DET regulator with current control.

This is the most efficient choice for the LRO because the operating point does not particularly vary along the mission limiting the dissipated current in the shunt. In order to fulfill the power demand during the eclipse phases, the PSE will also direct a portion of the sunlight-generated electrical power to the battery for energy storage. During the eclipse portion of the orbit the battery will provide all of the energy to the spacecraft [4]. The PSE consumes 43 W standby power and dissipates an additional 39 W under the nominal 890 W load condition [57]. The PSE is designed for single fault tolerance, which means that it is capable of satisfying the mission requirements also in the presence of a single anomaly or failure (see Section 6.1.3). The PSE is composed by four modules: the backplane module that serves as central hub connecting the other modules, the PSE Monitor Card (PMC) that controls communications and HK, the Solar Array Module (SAM) dedicated to SA power regulation and the Output Module (OM) assembly that provide resettable circuit breaker.

### 6.1.3 Battery

A single Lithium-Ion battery provides power to the spacecraft during eclipse phases or when the energy coming from the SA is insufficient to meet power requirements. In order to minimize electrical losses due to power converters and to maintain a stable bus voltage range, the battery is connected directly to the electrical bus. The battery energy storage capacity is expected to decrease during its operational lifetime: for this reason, the main battery selection and sizing criteria are aimed to meet a specific requirement of storage capacity at End of Life (EOL) while keeping the Depth of Discharge (DOD) in a limited range during nominal operations (see Section 6.3.2). The battery shall not overcome 30% DOD in nominal operations. The low DOD enables the battery to survive over the 5000 cycles expected during the mission with a significant margin. During lunar eclipse and in the launch phase a larger DOD is accepted (80% and 60% respectively) if required to meet the power needs. The battery is composed by Lithium-Ions cells arranged in 7 blocks each containing 12 strings of 8 cells. Even though no redundancy is present, this design ensures that cell failures (both open-circuit and short circuit) result in non-critical events, which correspond to a loss in capacity smaller than 1% [4]. In Table 6.2 the characteristic battery parameters have been reported.

BATTERY - PARAMETERS	VALUE
$E_m$ [Wh/kg]	140
$E_v$ [Wh/dm <sup>3</sup> ]	250
$\eta$	0.9

Table 6.2: Battery Characteristics [18]

## 6.2 Mission phases

The power demanded to the LRO's EPS varies depending on the mission phase, the operational requirements, and the specific activities to be performed by the spacecraft. For example, during the initial phases of the mission, when the spacecraft is undergoing various checkouts and tests, the power consumption would likely have been lower compared to when it is actively conducting scientific observations or transmitting data back to Earth. Table 6.3 reports the power consumption of the LRO per mode, according to the active systems and subsystems for each phase, determined from the ConOps, the previous sizing of other systems and reference [40].

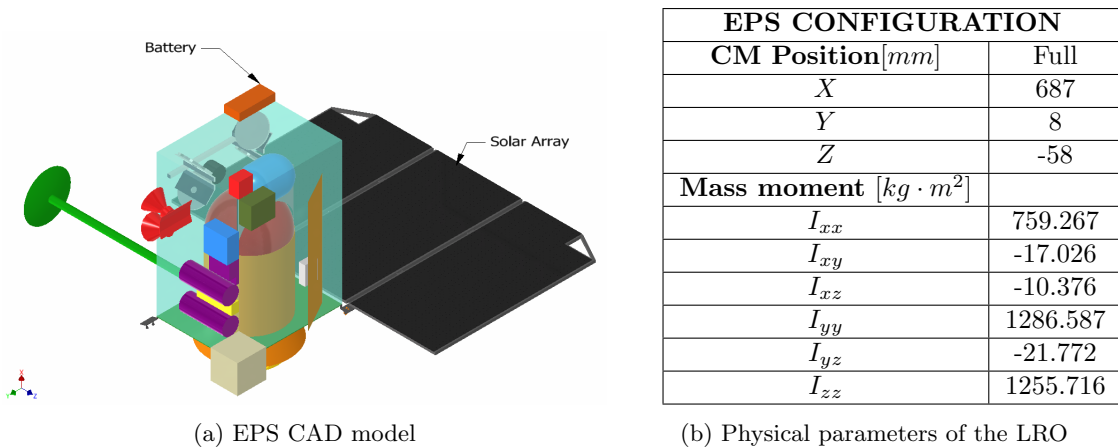
The  $\sim 0$  electrical power conditions means that the related contributions are negligible. For instance, since the OBDH subsystem is never switched completely off, it will always require a minimum amount of power. It should be noted that the power consumption increases as  $\beta$  increases, and arrives at its maximum when  $\beta = 90$  deg (see Section 6.3.1). The power consumptions listed in Table 6.3 correspond to this case in order to perform the sizing process with the worst possible case. Additionally, the spacecraft's distance to the sun is assumed to be constant due to the extremely small eccentricity of Earth's orbit around the sun and the fact that the LRO orbits the Moon on a circular orbit, which in turn orbits the Earth on an almost circular orbit.

## 6.3 Configuration & Sizing of the EPS

In Figure 6.2a the battery and the SA are shown, for simplicity the PSE is not considered. As defined in the PS and AOCS sections, each element has to be designed and positioned properly to avoid unwanted changes of moments of Inertia and positioning of the CM shown in Table 6.2b.

Power Demand [W]	Observing	LOI	Delta-V and Delta-H	Eclipse	Sun-Safe	Safehold
<b>PS</b>	0	58,1	48,8	0	0	0
<b>TTMTC</b>	110	35	35	0	0	0
<b>AOCS</b>	137	107	137	107	0	107
<b>PDE</b>	0	10	10	0	0	0
<b>TCS</b>	1032	1063	1166	1232	1317	977
<b>PL</b>	119,3	0	0	119,3	0	0
<b>OTHER</b>	50	$\sim 0$	$\sim 0$	$\sim 0$	25	$\sim 0$
<b>TOTAL</b>	<b>1448,3</b>	<b>1273,1</b>	<b>1396,8</b>	<b>1458,3</b>	<b>1342</b>	<b>1084</b>

Table 6.3: Power consumption per mode, per system



(a) EPS CAD model

(b) Physical parameters of the LRO

Figure 6.2: CAD model and physical parameters of the LRO

The sizing of the EPS components takes into account the worst case scenario for the power consumption of the spacecraft's subsystems, which comes when  $\beta = 90$  deg. If during this period a lunar eclipse takes place, and it is predicted to last longer than the nominal maximum occultation period of 48 min (during which the LRO goes into the eclipse mode), the orbiter enters the safeholding mode during which the non-essential systems are powered down [32].

### 6.3.1 Solar Array

Starting from the power requirements (highlighted in Table 6.3) and the worst case scenario duration of the charging and discharging cycles for the batteries of 65 and 48 minutes, respectively, the SA sizing has been performed. Typical line efficiency values for a DET configuration are taken as 0.85 and 0.65 for daylight and eclipse, respectively. In the process of sizing the area of the SA, the sun incidence angle must be considered. The LRO's SA has 2-dof control, and the evolution of the pointing of the panels is shown in Figures 6.3 and 6.4. The SA pointing accuracy is 2.8 deg, while the requirement is 5 deg [40]. The value of 5 deg is used since it represents a critical scenario for the sun incidence angle. The sizing of the SA is performed by computing the total power demand for the arrays (3358.8 W). Then, the specific power output at the beginning of life is calculated by considering the Sun's irradiance (1330 W), the BOL efficiency of the GaAs cells (0.3 [18]), the inherent degradation of the cells (0.77 [18]) and the targeted angle between the array surface and the sun direction (5 deg) to determine specific power produced under BOL conditions ( $306.06 W/m^2$ ). Lifetime degradation is considered for a mission duration of 14 months [40] and yearly degradation of 0.0375 [18], resulting in specific power at EOL of  $292.71 W/m^2$ .

The sized SA is composed by three panel frames containing a total of 89 modules. Inside each module, 2 strings composed by 24 GaAs cells in series are accommodated. These are arranged in a C-shape so that a compact structure is obtained, allowing to reduce the occupied volume when the orbiter is inside the LV's fairing. In Figure 6.5a and Table 6.5b the module structure and data are shown, which may differ from real mission data due to sizing assumptions, such as the individual cell performance parameters and the power generation requirement.

The number of modules computed is higher than the real case [4]. This is due to the conservative  $P_{EOL}$

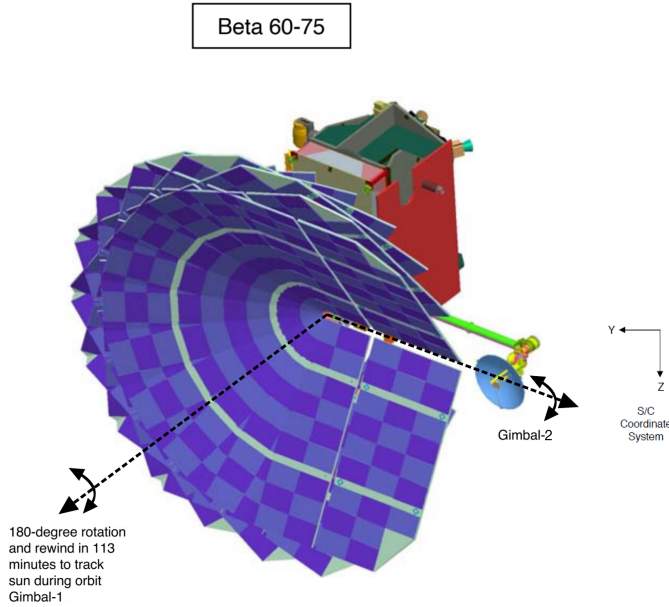


Figure 6.3: Evolution of the Gimbal-1 movement with respect to the true anomaly [40]

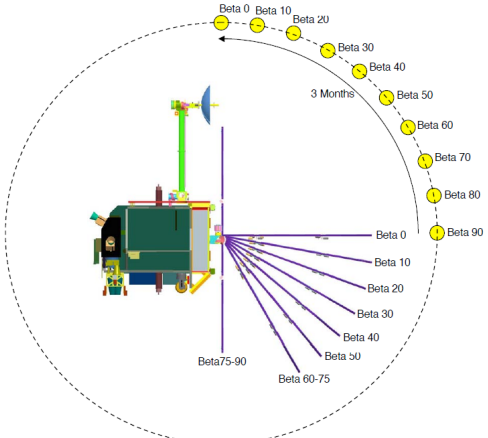


Figure 6.4: Evolution of the Gimbal-2 movement with respect to the  $\beta$  angle [40]

obtained in the previous steps. Additionally, the SA mass computed is near to the real one (36.4 kg [40]), but due to different number of modules taken into account a difference is obtained. The SA surface area obtained from the sizing process is  $\sim 15\%$  larger than the real  $A_{SA}$  ( $11.816 \text{ m}^2$ ) [58], related to the accumulation of margins and assumptions when performing the sizing.

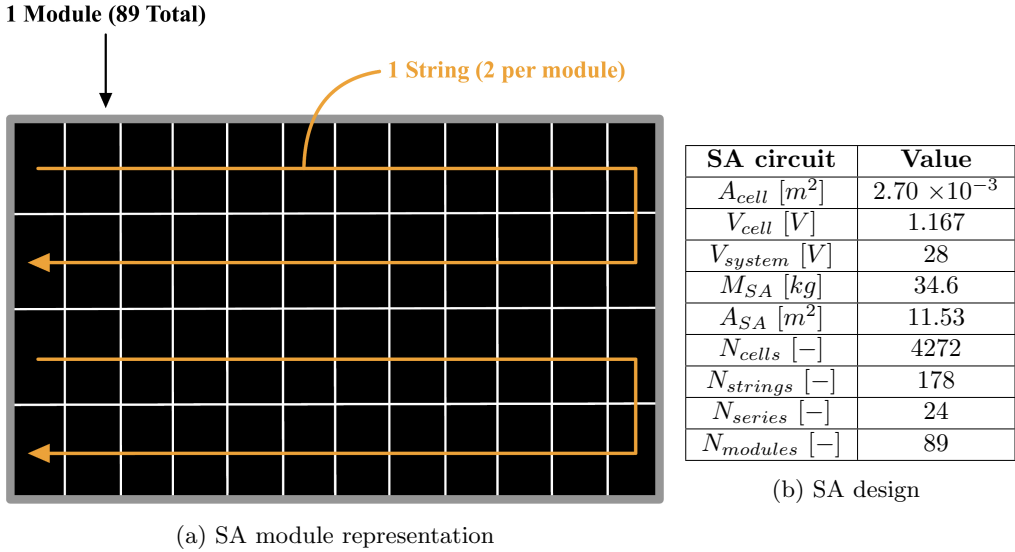
### 6.3.2 Battery

In order to perform the battery sizing, both the nominal and lunar eclipse conditions must be considered. When a lunar eclipse occurs, the LRO enters in safe-holding mode in which it operates with reduced capabilities for a period up to 160 minutes [40]. Table 6.4 shows the data used to size the battery.  $DOD_{normal}$  was set to 30% as the sizing parameter, but it changed due to the determination of quantities that must be integer numbers, such as the amount of cells in a circuit. It should be noted that  $DOD_{eclipse}$  is computed in order to check the capability of the battery of supplying the required energy during the seldom-occurring lunar eclipses. If it was larger than 80%, the capacity of the battery would have been enlarged in order to keep  $DOD_{eclipse}$  under this value [32].

Battery data	Value
<b>Lunar Occultation</b>	
$P_{R,normal} [\text{W}]$	1458.3
$T_{R,normal} [\text{h}]$	0.8
$DOD_{normal}$	29.1%
<b>Lunar Eclipse Safeholding</b>	
$P_{R,eclipse} [\text{W}]$	1084
$T_{R,eclipse} [\text{h}]$	2.67
$DOD_{eclipse}$	72%

Table 6.4: Battery Sizing Data

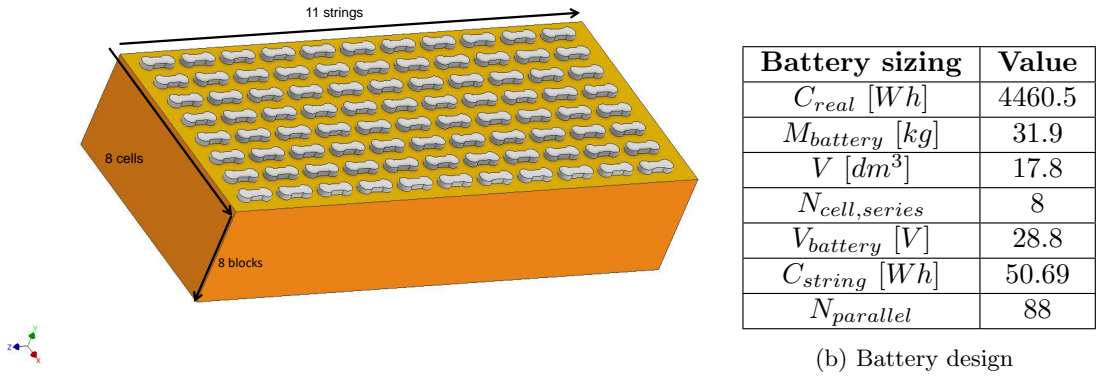
The battery has a nominal voltage of 28.8 V, with each individual cell having a voltage of 3.6 V 6.6b. By dividing the nominal voltage by the voltage per cell, the number of strings is determined to be 8. To fulfill the required capacity defined from mission analysis the battery is composed by eight blocks positioned in parallel: each block is constructed with 11 strings of 8 cells, to give a total of 704 cells as shown in Figure 6.6a. The obtained values are comparable to the real one, in fact the LRO's battery is composed of seven blocks of 12 strings of cells in series, with a total of 672 cells. The difference is related to the higher capacity considered (151.36 A-h), while the real one is equal to 100 A-h. Another possible comparison is the real mass and the computed one. The mass obtained in the sizing process, as reported in Table 6.6b, is comparable with the real mass of 36.4 kg [4], it corresponds to the mass of only the cells



(a) SA module representation

Figure 6.5: SA module design and parameters

and does not consider the case or structure. By using a typical value of 0.8 for the package efficiency and a typical value of 2.2 Ah for capacity of a single cell, the capacity of a string can be determined to be 50.69 Wh. The number of string (equal to 88) is obtained dividing the total capacity by the capacity of a single string hence the capacity result is 4460.5 Wh.



(a) Battery CAD model

Figure 6.6: Battery model and design parameters

## 6.4 Mass budget

The mass budget of the EPS is shown in Table 6.5. As previously stated in Section 6.1, the introduction of a DET architecture increases the overall mass of the EPS and should be considered additionally. Cables mass density is obtained from empirical statistical models considering the current equal to 66 A (computed from the Joule power law) [18]. For the contribution of the cables, 10% of the total EPS mass is considered. The mass budget is shown in Table 6.5.

<b>Mass [kg]</b>	<b>Value</b>
$M_{battery} [kg]$	30.864
$M_{SA} [kg]$	34.334
$M_{cables} [kg/m]$	0.3
$M_{PSE} [kg]$	3
$M_{EPS} [kg]$	71.72

Table 6.5: Mass budget

# Chapter 7

## Configuration

### Change log

- Sec 7.1.1 pp 46: Detailed description of the internal components.

## 7.1 Orbiter configuration

The LRO design configuration is composed by the sized internal and external components. Considering the case sizing, the discrepancies with respect to the real S/C are related to the rough approximations performed and to the non-perfect knowledge of the components arrangement inside the orbiter. Sections 7.1.1 and 7.1.2 discuss the configuration of the onboard components.

### 7.1.1 Internal configuration

The temperature management is the main driver for the arrangement of the internal components, reducing as much as possible the use of heaters. In fact, the temperature control is mainly focused on passive devices, utilizing heat pipes to enlarge cooling capacity without exploiting moving parts. The instruments with higher power request are fixed on the bottom part of the avionics module to facilitate the power dissipation. The propulsion system is the main supporting structure in LRO as shown in Figure 7.2. In the bottom part are attached the thrusters while the side walls exchange heat only through radiation. The main aluminum structure has the purpose of protecting all the components of the spacecraft providing electrical grounding and shielding to the subsystem from solar wind and cosmic rays. Pressurizer tank is offset from the LRO's center line and situated closer to the +Y to allow the positioning of the reaction wheels. The SA is also mounted on -Y face, as shown in Figure 7.2, therefore this face is the most critical for solar radiations. For this reason, a rad-hard radiation cover is mounted over the avionics module leaving space to avoid conduction towards the internal components. This cover acts as the panel upon which the SA are folded against in launch configuration.

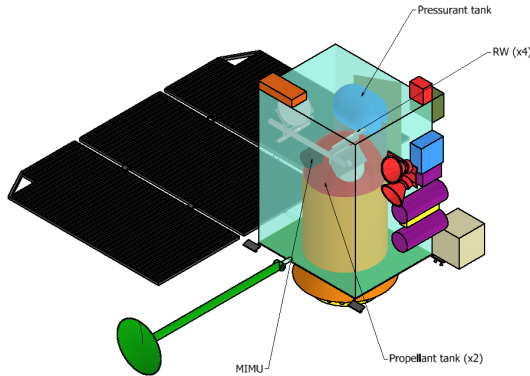


Figure 7.1: LRO internal architecture

### 7.1.2 External configuration

The majority of the external components are the payload instruments. They are projected to resist to the environment and also perform scientific observation, not possible if located inside the orbiter. The location of each component is constrained due to mission analysis, according to their pointing direction, functionalities and ConOps as described in Table 7.1. The same happens for the SA and HGA, these components must be located externally to accomplish their tasks, as represented in Figure 7.2. LOLA, LROC, LAMP and star trackers are placed nearby because are connected to the *Instrument bench module* to fulfill the high precision pointing requirement of the instruments. Instead, the other instruments are attached to the main orbiter structure.

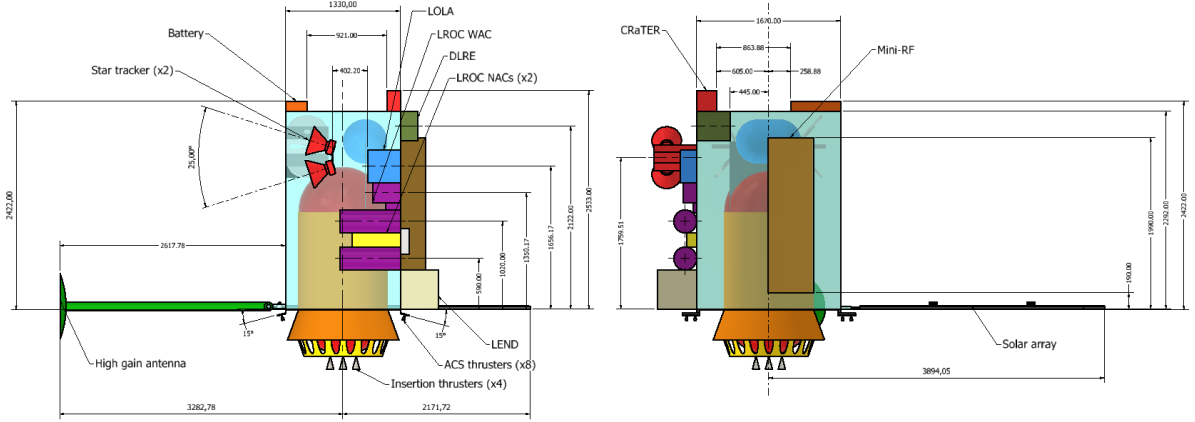


Figure 7.2: LRO overall dimensions

## 7.2 Launcher interface

Using the final CAD model and launch mass<sup>1</sup> (see the appendix), the LV payload fairing was selected according to the final dimensions of the modelled spacecraft and the launch service provider [3], which was the Extended Payload Fairing (EPF) [40]. This is the intermediate payload fairing available for the Atlas V 400 series of rockets, which provides the high  $C_3$  for the Atlas V 401 while minimizing the unused space inside the fairing. Inside the fairing module, the LRO adopts a specific configuration. The 3 solar array panels are folded one on top of the other and rotated by 90 deg so that they lay on the orbiter external surface. This allows to reduce the occupied volume, to prevent damages due to launch vibrations and to keep the center of mass in a suitable position for the whole launch duration. For the same reasons, the HGA is also rotated and brought closer to the LRO body. On the bottom side, the real orbiter is connected through the fairing adapter to the Centaur Upper Stage. The LRO is attached to LCROSS via a payload adapter, and the LCROSS is in turn connected to the Centaur Upper Stage. The adapters and LCROSS spacecraft are not represented in Figure 7.3, which shows the launch configuration of the LRO inside the EPF.

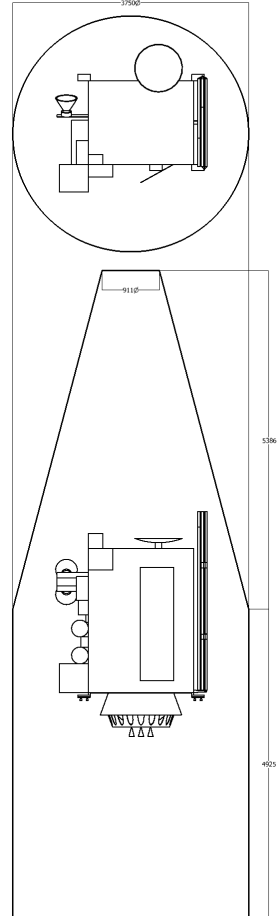


Figure 7.3: LRO folded configuration inside the Atlas V's EPF

<sup>1</sup>The final dry mass from the CAD model, references for the components used and sizing processes is 630.6 kg, which is 387.4 kg lighter than the real world case. This is due to several factors, such as the lack of modelling in detail the spacecraft's structure and other secondary components that are part of the subsystems but are not included in the sizing processes or referenced in the literature.

DEVICE	POSITION [4]	ConOps [5]
<b>EXTERNAL</b>		
<b>Solar Array</b>	Movable solar array allows to track the position of the Sun having an high power generation	Deployment Supply power in daylight
<b>Battery</b>	Positioned outwardly on the X face to balance global inertia of the s/c.	Battery charging Supply power in eclipse
<b>HGA</b>	Located in the -z direction with two DOF gimbals. Ensure accurate payload pointing also during communication windows.	Deployment Tracking Communications
<b>Insertion Thrusters</b>	Located in -X direction and align to the CM in order to avoid attitude control during LOI.	Perform LOI manouvers
<b>AOCS Thrusters</b>	Located in -X direction inclined of 15° to shift the thrust axis away from the CM.	Perform ACS burns
<b>LEND</b>	Locate in the corner opposite to the solar array.	Provides space radiation environment measurements [2]
<b>LROC NACs</b>	Located on Y face.	Capture images [2]
<b>LROC WAC</b>	Located on Y face.	Capture images [2]
<b>LAMP</b>	Located on Y face.	Provide PSR mapping [2]
<b>LOLA</b>	Located on Y face.	Analyze lunar surface elevation [2]
<b>DLRE</b>	Located on Z face.	Provide orbital thermal mapping [2]
<b>CRaTER</b>	Located on X face.	Characterize lunar radiation and potential biological impacts [2]
<b>MINI-RF</b>	Located in the Z face.	High resolution imagery of PSR [2]
<b>Star Trackers</b>	Located in Y face, pointing along the Zenith towards DS.	Refined attitude determination Maintain pointing direction
<b>CSSs</b>	Locate to give a global spherical field of view of the outer space.	Coarse attitude determination
<b>INTERNAL</b>		
<b>RWs</b>	Pyramid configuration to increase the robustnesses of the control system.	De-Spin Perform attitude changes
<b>MIMU</b>	Located on -Z face.	Provide attitude informations
<b>Heaters</b>	Displaced in critical thermal point.	Provide thermal energy Disable when not required
<b>Tanks</b>	Located in the central body in order to reduce inertia moments and increase the orbiter stability.	Provide energy source (propellant)

Table 7.1: LRO internal & external components

# Chapter 8

## On-Board Data Handling subsystem

### 8.1 OBDH Architecture

The OBDH subsystem is subdivided in three main area:

- **Telemetry generation and command processing.** The C&DH utilizes two similar designs on a single assembly, with each design dedicated to a single band.
- **Collection of science data from instruments.** The C&DH provides timing synchronization to all the instruments as well as providing a mission unique interface to the LAMP instrument through HKIO. The Federated bus architecture has been adopted, granting a reduced *trouble shooting* time and improving the reliability. The SpaceWire and MIL-STD-1553 are used for their expandable performance and scalability [59].
- **Storage of science and housekeeping data between telemetry downlink passes.** Data collected from the instruments and the avionics housekeeping data is kept within this storage system prior to playback during a telemetry pass.

Figure 8.1 illustrates the top-level block diagram of the C&DH.

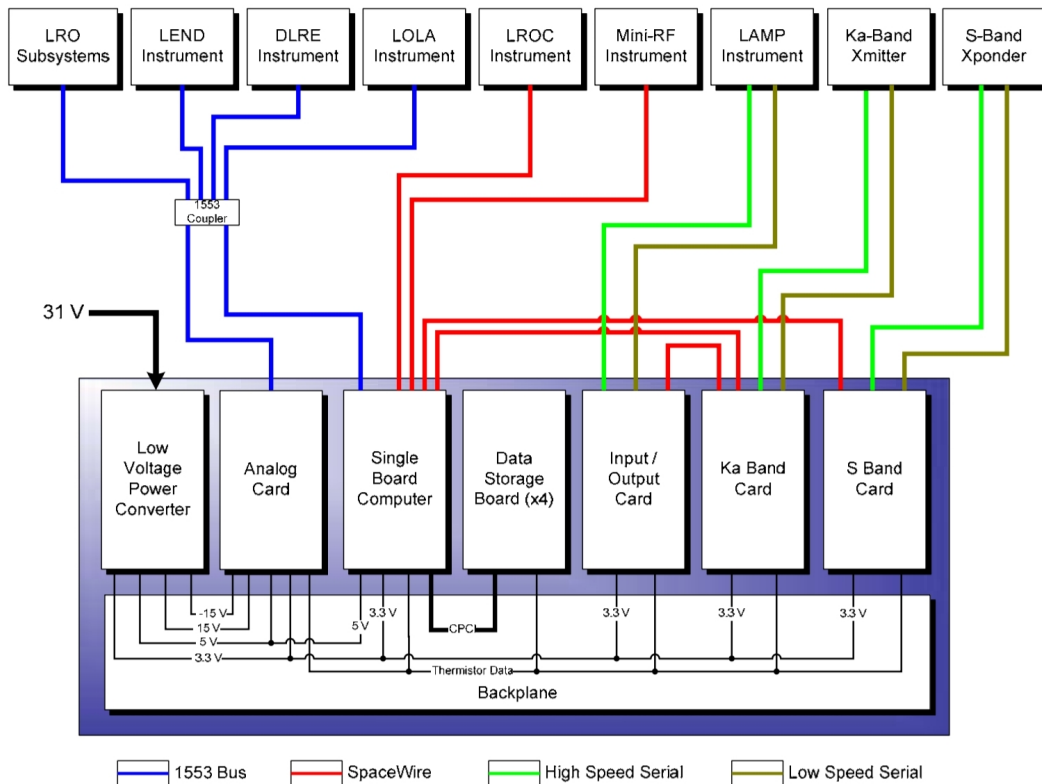


Figure 8.1: OBDH architecture

**Single Board Computer (SBC) and Bus architecture** The main characteristics of the SBC are reported in Table 8.1. The SBC is the processing platform for the flight software and the attitude control software. The onboard system architecture uses the SpaceWire bus in support of high-speed interfaces (LROC, Mini-RF, Ka-Band Comm Card, S-Band Comm Card and LAMP), while the MIL-STD-1553B low-speed bus is used for LEND, DLRE, CRaTER, LOLA, ACS, PSE, and the propulsion subsystem. The adoption of the standard MIL-STD-1553B allows a more efficient identification and isolation of the anomalies increasing the reliability. However, all the component interfaces connected shall be design properly.

The two high-data-rate instruments onboard LRO are the LROC (LRO Camera) and Mini-RF. The spacecraft design connected both instruments to the same SpaceWire bus to send data to the SSDR (Solid State Data Recorder). The design of the light software that managed data on the bus precludes both instruments from operating simultaneously. This was not anticipated to be an issue due to the limited operational time of Mini-RF in the mission baseline plan [1].

Elements	Characteristics/model	Description
Processor	RAD750	-
Frequency	133 MHz	-
Radiation resistance	50 Krads	-
SRAM	36 MByte	To store executable code and housekeeping data
SUROM	64 kByte	To store essential bootstrap code(?)
EEPROM	4 MByte	To store application code

Table 8.1: SBC characteristics and properties [59]

**Input / Output Card** The HKIO is a mission unique board that provides three functions: distribute the 1 pulse per second signal, maintain the mission elapsed timer and provide the LAMP specific interface. LAMP is derived from an earlier instrument used on the New Horizons, therefore its specific interface was not altered to reduce schedule risk and cost.

**Multi-Function Analog Card** The MAC provides all analog connectivity for the C&DH: internal telemetry, voltage monitoring, internal thermistors, platinum resistance thermometers, hinge potentiometers, coarse sun sensors, and pressure transducers. The MAC digitizes all the analog data, generates telemetry and receives commands over the 1553 bus.

**Data Storage Boards** Four DSBs are present on board which handle the storage and the retrieval of files. In BOL the Data storage boards provide 48 GByte of memory capacity ensuring an autonomy of 17.5 hours before downloading the scientific and telemetry data on ground. All the data transfer of the DSBs take place using PCI interface through the backplane connector.

**Ka-Band / S-Band Communications Cards** The Ka-Comm card provides high-speed telemetry to Earth using Ka-Band frequencies. The S-Comm card provides telemetry and receive commands to and from Earth using S-Band frequencies. Both are connected to the SBC via a SpaceWire link. The data from the SBC flows directly into the Ka-Comm card at the SpaceWire link rate of 132 Mbps (the data rate is 100 Mbps) while for the S-Comm card the link rate is 10Mbps (the maximum data rate is 1 Mbps).

Once the data is received from the SBC, the Comm cards proceed to encode them for transmission. The Ka-Comm card also provides command and control and receives housekeeping telemetry from the Ka-Band transmitter itself. The S-Comm card accepts CCSDS telecommands from the S-Band transponder and is able to establish time correlation with the ground stations.

**Low Voltage Power Converter** The LVPC installed on board is capable to convert an input voltage from 21 V DC to 35 V DC in 3.3 V DC, 5 V DC and  $\pm 15$  V DC. Moreover, it contains relays capable to drive power for several components of LRO's RF system (i.e. the S-Band antenna transfer switch and the TWTA power relay).

**Backplane** The backplane provides interconnectivity for the nine cards in the LRO C&DH System. These cards are connected through unique interface and include the S-Band and Ka-Band communication

cards, the HKIO card, the MAC, the LVPC, the SBC, and four DSB cards. The backplane also provides a compact PCI bus interface between the SBC and the four DSBs and is rated for 33 MHz data transfers.

**Enclosure** The C&DH enclosure acts as the mechanical housing (Table 8.2) for the C&DH unit and contains all of the C&DH hardware assemblies.

Dimensions [cm]	40.6 (L)	29.2 (W)	24.8 (H)
Mass [kg]	20.86		

Table 8.2: OBDH hardware assembly [59]

## 8.2 OBDH Sizing

The aim of this section is to identify and validate the onboard memory size and the SBC features. The first step for the sizing of the OBDH subsystem is the identification of the functions [36]. For all the S/C subsystem elements the processed data, code and instruction are identified. The real value of IPS is estimated by similarity for each functions assuming the operating frequency. In first approximation, the order of magnitude of the frequencies are estimated according to statistical values, as reported in Table 8.3. For the OS elements and for the ADCS parts that operates at high precision the frequency is assumed equal to the one of the MIMU. According to [60] the RWs dynamics and the MIMU response operate at 6 and 7 Hz respectively, therefore a conservative values of 10 Hz is assumed as the higher acquisition frequency onboard. This value is really close to the typical one, therefore it is considered as acceptable for the preliminary design. For the relatively slow time varying functions the frequency is reduced, according to typical frequency values. All the subsystem are considered although EPS and TCS

High	Medium	Low
10	1	0.1

Table 8.3: Frequency order of magnitude [Hz]

are characterized by very low data budget. For the PS thrusters the typical values [18] of code and data are scaled according to the engine thrust. The LRO has level 2 autonomy [59] therefore simple autonomy is assumed in the functions. The system estimates the attitude of the S/C from a six-state Kalman filter that has been included in the functions [36]. The Kalman filter throughput is dominant over the other elements due to the huge quantity of data managed. The functions contributions are reported in Table 8.4.

For the OS functions the useful data are reported in Table 8.5. The Run-Time Kernel and Math Utilities elements throughput value are already included in functions which use these features [36]. For the throughput estimates of the Typical Onboard Operating System Software the number of task scheduled per second  $n$  and the number of data words handled per second  $m$  shall be determined. According to [36]  $n = 300$ , obtained considering 3-4 tasks for each major function assumed at its frequency. The  $m$  value is assumed equal to 1000 words/second [18], while 5 Input-Output devices are considered to take into account the multiplicity of the sensors and the bus link [36].

For all the subsystems the total values are reported in Table 8.6. A 400% margin is applied according to [36].

The total ROM, RAM and throughput are computed, results are reported in Table 8.7.

The requested ROM is compatible with the RAD-750 ROM, while the RAM is lower. This difference can be related to the not considered payload data and to the statistical values assumed for the functions. The total throughput exceeds the maximum value due to the large margins considered that can be reduced at launch [36], moreover the frequency adopted allows to obtain only a rough estimate of the functions KIPS.

Components	Number	Code [Kwords]	Data [Kwords]	Typical KIPS	Typical frequency [Hz]	Acquisition frequency [Hz]	Estimated KIPS
<b>ADCS</b>							
Star Traker	2	2	15	2	0,01	1	200
Coarse sun sensor	10	0.5	0.1	1	1	0.1	0.1
MIMU	1	0.8	0.5	9	10	10	9
Kinematic integration	1	2	0.2	15	10	10	15
Error determination	1	1	0.1	12	10	10	12
Thruster control	8	0.6	0.4	1.2	2	10	6
RW control	4	1	0.3	5	2	10	25
Kalman Filter	1	8	1	80	0.01	10	80000
Complex eph	1	3.5	2.5	4	0.5	10	80
Orbit propagation	1	13	4	20	1	10	200
<b>PS</b>							
Main Engine	4	0.27	0.3375	1.125	0.1	0.1	1.125
ACS Engine	8	0.066	0.0825	0.275	0.1	0.1	0.275
Pressure Trasducer	2	0.8	1.5	3	0.1	0.1	3
Latch Valves	7	0.8	1.5	3	0.1	0.1	3
Pressure Regulator	1	0.8	1.5	3	0.1	0.1	3
<b>EPS</b>							
Voltage control	1	1.2	0.5	5	1	0.1	0.5
Current control	1	1.2	0.5	5	1	0.1	0.5
<b>TCS</b>							
Thermal control	1	0.8	1.5	3	0.1	0.1	3
<b>TTMTC Subsystem</b>							
Command processing	1	1	4	7	10	1	0.7
Telemetry processing	1	1	2.5	3	10	1	0.3
<b>Other functions</b>							
Simple Autonomy	1	2	1	1	5	1	0.2
Fault Detection	1	4	1	15	5	1	3
Fault Correction	1	2	10	5	5	1	1

Table 8.4: Size and Throughput Estimates for Common Onboard Applications

Components	Number	Code [Kwords]	Data [Kwords]	KIPS
Executive	1	3.5	2	0.57
Run Time Kernel	1	8	4	-
I/O Device Handlers	5	2	0,7	1.75
Built-In Test and Diagnostic	1	0.7	0,4	0.57
Math Utilities	1	1.2	0,2	-

Table 8.5: Size and Throughput Estimates for Operating System functions

	ADCS	PS	EPS	TCS	TTMTC	OS+Other functions	Total
Throughput [KIPS]	404325	183.5	5	15	6,5	248.5	404886
Code [Kwords]	230.5	48.04	12	4	15	157	466.54
Data [Kwords]	218.5	85.05	5	7.5	45	110.5	471.55

Table 8.6: Total subsystem Size and Throughput estimate assuming 400% margin [36]

	ROM [MB]	RAM [MB]	Throughput [MIPS]
Computed	3.64	7.33	395.30
RAD-750	4	36	300

Table 8.7: ROM, RAM and Throughput comparison [59]

# Bibliography

- [1] ESA. *EO portal LRO*, <https://www.eoportal.org/satellite-missions/lro#eop-quick-facts-section>. 2013.
- [2] Craig Tooley. “Lunar Reconnaissance Orbiter Project Overview & Status”. In: *NASA Goddard Space Flight Center*, [https://lunar.gsfc.nasa.gov/library/lro\\_plenary\\_session.pdf](https://lunar.gsfc.nasa.gov/library/lro_plenary_session.pdf) (2006).
- [3] United Launch Alliance. “Atlas V Launch services user’s guide”. In: *Lockheed Martin Commercial Launch Services* (2010).
- [4] Craig R Tooley et al. “Lunar Reconnaissance Orbiter mission and spacecraft design”. In: *Space Science Reviews* 150 (2010), pp. 23–62.
- [5] Washington University PDS geosciences node. *Lunar Reconnaissance Orbiter*, [https://pds-geosciences.wustl.edu/missions/lro/docs/lro\\_insthost.txt](https://pds-geosciences.wustl.edu/missions/lro/docs/lro_insthost.txt).
- [6] NASA. In: *LRO Propulsion System Design & On-Orbit Operations*. NASA Goddard Space Flight Center, 2012, pp. 1–15.
- [7] Mark Beckman. “Mission design for the lunar reconnaissance orbiter”. In: *29th Annual AAS Guidance and Control Conference*. AAS-07-057. 2007.
- [8] Erwan Mazarico et al. “Orbit determination of the lunar reconnaissance orbiter”. In: *Journal of Geodesy* 86 (2012), pp. 193–207.
- [9] United Launch Alliance. *ROCKET RUNDOWN*, <https://www.ulalaunch.com/docs/default-source/rockets/atlas-v-and-delta-iv-technical-summary.pdf>. 2022.
- [10] NASA. *Space Launch Report*, <https://sma.nasa.gov/LaunchVehicle/assets/space-launch-report.pdf>. 2018.
- [11] Jet Propulsion Laboratory. *JPL Solar System Dynamics*, <https://ssd.jpl.nasa.gov>.
- [12] NASA Goddard Space Flight Center. *The LRO Instruments*, <https://lunar.gsfc.nasa.gov/instruments.html>. 2022.
- [13] National Institute of Standards and Technology. *NIST Chemistry WebBook*. 2023. URL: <https://webbook.nist.gov/chemistry/>.
- [14] MOOG Space and Defence Group. *AMPAC, MONARC-90*, <https://www.satcatalog.com/component/monarc-90lt/>. 2018.
- [15] Aerojet Rocketdyne. *Aerojet, MR106L*, <https://www.satcatalog.com/component/mr-106l-22n/>. 2020.
- [16] NORTHROP GRUMMAN. *Propellant tank*, <https://www.northropgrumman.com/space/diaphragm-tanks-data-sheets-sorted-by-part-number/>.
- [17] ASME Boiler and Pressure Vessel Code, Section VIII, Division 1. New York, NY, 2019.
- [18] Lavagna Michèle Roberta. *Space Systems Engineering and Operations Course Notes*. Politecnico di Milano. 2023.
- [19] Fabrice Lacroix Vadim Allheily. “An experimental method to assess the thermo-mechanical damage of CFRP subjected to a highly energetic 1.07 mm-wavelength laser irradiation”. In: (2016).
- [20] Dept of Materials Science and Metallurgy, University of Cambridge. *Fibre Composites*. [https://www.doitpoms.ac.uk/tlp/lib/fibre\\_composites/strength.php](https://www.doitpoms.ac.uk/tlp/lib/fibre_composites/strength.php). [Online; ultima consultazione: giornomeseanno]. s.d.
- [21] George Lubin. *Composite Materials: Engineering and Science*. Boca Raton, FL: CRC Press, 1998. ISBN: 9780849384223.

- [22] Mario Salvadori. "Composite Materials: Properties as Influenced by Phase Geometry". In: *Journal of Materials Education* 6.1 (1984), pp. 37–44.
- [23] National Aeronautics and Space Administration. *Standard for Safety Design of Pressure Vessels for Human Occupancy*. Tech. rep. NASA-STD-8719.9. NASA, 2016.
- [24] Keller Druckmesstechnik AG. *Series 33 X — Series 35 X: High Precision Pressure Transmitters*. <https://download.keller-druck.com/api/download/w7JDRX63Cnx4BseMSQkdqW/en/2021-01.pdf>. Accessed: May 4, 2023. 2021.
- [25] Moog Incorporated. *50E920 Liquid Valve*. <https://www.moog.com/literature/ICD/50e920.pdf>. Accessed: May 5, 2023. 2013.
- [26] James R Wertz and Wiley J Larson. *Spacecraft attitude determination and control*. 3rd. Springer Science & Business Media, 2011, pp. 187–188.
- [27] Neerav Shah, J Roger Chen, and Joseph A Hashmall. "A General Closed-Form Solution for the Lunar Reconnaissance Orbiter (LRO) Antenna Pointing System". In: *AIAA Guidance, Navigation and Control (GN&C) Conference*. 2010.
- [28] C3S ELECTRONICS DEVELOPMENT LLC. *C3S PLATFORM DATA SHEET*, <https://www.satcatalog.com/component/antenna-system/>. 2021.
- [29] Planetary Data System. "Radio Science Subsystem, instrument overview". In: (2022). URL: [https://pds.nasa.gov/ds-view/pds/viewInstrumentProfile.jsp?INSTRUMENT\\_ID=RSS&INSTRUMENT\\_HOST\\_ID=LRO](https://pds.nasa.gov/ds-view/pds/viewInstrumentProfile.jsp?INSTRUMENT_ID=RSS&INSTRUMENT_HOST_ID=LRO).
- [30] Ann Nicholson et al. "NASA GSFC lunar reconnaissance orbiter (LRO) orbit estimation and prediction". In: *SpaceOps 2010 Conference Delivering on the Dream Hosted by NASA Marshall Space Flight Center and Organized by AIAA*. 2010, p. 2328.
- [31] David E Smith et al. "The lunar orbiter laser altimeter investigation on the lunar reconnaissance orbiter mission". In: *Space science reviews* 150 (2010), pp. 209–241.
- [32] NASA. *LRO Mission Concept of Operations Summary*. 2005.
- [33] Rick Saylor. "Lunar Reconnaissance Orbiter Flight Operations Review (FOR)". In: (2009). URL: <https://www.yumpu.com/en/document/read/11436648/lunar-reconnaissance-orbiter-mission-operations-review-mor->.
- [34] David D Morabito. "Dynamic telemetry link advantage when tracking a lunar orbiter with a 34-m antenna at 2.3 GHz and 8.4 GHz". In: *The Interplanetary Network Progress Report* 42 (2015), p. 200.
- [35] NASA. *Lunar Reconnaissance Orbiter Project Mission Requirement Document*. 2008. URL: [https://snebulos.mit.edu/projects/crater/file\\_cabinet/0/01003/01003\\_01\\_rDm.pdf](https://snebulos.mit.edu/projects/crater/file_cabinet/0/01003/01003_01_rDm.pdf).
- [36] Wiley J Larson, James Richard Wertz, et al. *Space Mission Analysis and Design*. Vol. 3. Springer, 1992.
- [37] Jim Simpson et al. "Integration and Testing of the Lunar Reconnaissance Orbiter Attitude Control System". In: (2011). doi: 10.1109/AERO.2011.5747274.
- [38] Franco BOLDRINI. *THE OFFICINE GALILEO AUTONOMOUS STAR TRACKER*.
- [39] Honeywell. *MINIATURE INERTIAL MEASUREMENT UNIT: Proven performer for satellite and deep-space-probe applications*.
- [40] Arlin Bartels et al. "LRO Preliminary Design Review Payload System Overview". In: (2006). URL: <https://studylib.net/doc/25389652/day-2>.
- [41] Neerav Shah et al. "Launch and Commissioning of the Lunar Reconnaissance Orbiter (LRO)". In: *2010 American Astronautical Society (AAS) Guidance and Control (G and C) Conference*. 2010.
- [42] S. Alan Stern. *The Lunar Atmosphere: History, Status, Current Problems, and Context*. Tech. rep. NASA, Southwest Research Institute, Jan. 1997.
- [43] L. L. Hood et al. "Magnetic fields and lunar exploration". In: *Space Science Reviews* 135.1-4 (2008), pp. 187–202.
- [44] Hamid K Rassoul. "The Earth's Magnetic Field". In: *The Earth's Ionosphere: Plasma Physics and Electrodynamics* (2006), pp. 1–32.
- [45] Philip Calhoun. "Solar Array Disturbances to Spacecraft Pointing during the Lunar Reconnaissance Orbiter (LRO) Mission". In: *AIAA GNC Conference* (2010).

- [46] Joseph C. Garrick Philip C. Calhoun. “Observing Mode Attitude Controller for the Lunar Reconnaissance Orbiter”. In: *20th International Symposium on Space Flight Dynamics* (2007).
- [47] Franco Bernelli Zazzera. *Spacecraft Attitude Dynamics Course Notes, Part 2: Attitude sensors and actuators, attitude determination*. Politecnico di Milano. 2022.
- [48] Charles Baker et al. “Lunar Reconnaissance Orbiter (LRO) rapid thermal design development”. In: *Heatpipes for Space Applications International Conference*. 2009.
- [49] Pradeep Bhandari. “Robust thermal control of propulsion lines for space missions”. In: (2016).
- [50] Charles Baker. “LRO General Thermal Subsystem Specification”. In: (2005). URL: <https://studylib.net/doc/15969055/draft-lunar-reconnaissance-orbiter--lro---general-thermal....>
- [51] Erik Stalcup. “Lunar Thermal Environment”. In: (2021). URL: [https://www.nasa.gov/sites/default/files/atoms/files/ericstalcup\\_lunar\\_thermal\\_environment\\_v2.pdf](https://www.nasa.gov/sites/default/files/atoms/files/ericstalcup_lunar_thermal_environment_v2.pdf).
- [52] Craig Tooley. “Lunar Reconnaissance Orbiter Spacecraft and Objectives”. In: (2006). URL: <https://lunar.gsfc.nasa.gov/library/tooley-scobjectives-51906.pdf>.
- [53] Charles Baker et al. “Lunar Reconnaissance Orbiter (LRO) Thermal On-Orbit Performance”. In: *40th International Conference on Environmental Systems*. 2011, p. 6000.
- [54] Eugene A Avallone. *Standard handbook for mechanical engineers*. 1987.
- [55] Dunmore. *Germanium Coated Kapton Film datasheet*. URL: <https://www.dunmore.com/products/germanium-polyimide-film.html>.
- [56] Mouser Electronics. *Thermistor YSI 2.252 kohm*. URL: <https://eu.mouser.com/c/circuit-protection/thermistors/ntc-thermistors/?product%5C%20type=NTC%5C%20Thermistors&resistance=2.252%5C%20kOhms&pg=2>.
- [57] Amri Hernandez-Pellerano et al. “A High Power Density Power System Electronics for NASA’s Lunar Reconnaissance Orbiter”. In: *7th International Energy Conversion Engineering Conference*. 2009, p. 4547.
- [58] Diane Yun. “Electrical Power System Architecture For In-House NASA/GSFC Missions”. In: (2006).
- [59] Quang Nguyen et al. “A high performance command and data handling system for NASA’s lunar reconnaissance orbiter”. In: *AIAA SPACE 2008 Conference & Exposition*. 2008, p. 7926.
- [60] Philip C Calhoun and Joseph C Garrick. “Observing mode attitude controller for the lunar reconnaissance orbiter”. In: *Proceedings of the 20th international symposium on space flight dynamics*. 2007.
- [61] Quang H. Nguyen et al. “A High Performance Command and Data Handling System for NASA’s Lunar Reconnaissance Orbiter”. In: 2008.
- [62] H. E. Spence et al. “CRaTER: The Cosmic Ray Telescope for the Effects of Radiation Experiment on the Lunar Reconnaissance Orbiter Mission”. In: *Space Science Reviews Vol. 150*. 2010.
- [63] NASA GSFC. *LROC Specs*, <http://lroc.sese.asu.edu/about/specs>. 2013.
- [64] IG Mitrofanov. “Lunar Exploration Neutron Detector for the NASA Lunar Reconnaissance Orbiter”. In: *Space Science Reviews Vol. 150*. 2010.
- [65] D. A. Paige et al. “The Lunar Reconnaissance Orbiter Diviner Lunar Radiometer Experiment”. In: *Space Science Reviews Vol. 150*. 2010.
- [66] NASA JPL. *MCS*, <https://mars.nasa.gov/mro/mission/instruments/mcs/>.
- [67] GR Gladstone. “LAMP: The Lyman Alpha Mapping Project on NASA’s Lunar Reconnaissance Orbiter Mission”. In: *Space Science Reviews Vol. 150*. 2010.
- [68] S Nozette. “The Lunar Reconnaissance Orbiter Miniature Radio Frequency (Mini-RF) Technology Demonstration”. In: *Space Science Reviews Vol. 150*. 2010.

## Acronyms

<b>ACS</b>	Attitude Control System	<b>HGA</b>	High Gain Antenna
<b>AOCS</b>	Attitude Orbit and Control System	<b>HGF</b>	High-pressure Gas Filter
<b>ADCS</b>	Attitude Determination and Control System	<b>HKIO</b>	Housekeeping Input/Output Board
<b>BARF</b>	Body Axes Reference Frame	<b>HP</b>	Heat Pipes
<b>BER</b>	Bit Error Rate	<b>HPLV</b>	High-Pressure Latch Valve
<b>BOL</b>	Beginning Of Life	<b>HPR</b>	High-Pressure Regulator
<b>BPSK</b>	Binary Phase Shift Keying	<b>HK</b>	Housekeeping
<b>C and DH</b>	Command and Data Handling	<b>IMU</b>	Inertial Measurement Unit
<b>CAD</b>	Computer-Assisted Design	<b>IPS</b>	Instruction Per Second
<b>CCSDS</b>	Consultative Committee for Space Data Systems	<b>IR</b>	Infrared
<b>CFRP</b>	Carbon Fibers-Reinforced Plastic	<b>IRU</b>	Inertial reference unit
<b>CM</b>	Centre of Mass	<b>LAMP</b>	Lyman Alpha Mapping Project
<b>COPV</b>	Composite Overwrapped Pressure Vessel	<b>LCROSS</b>	Lunar CRater Observation and Sensing Satellite
<b>CRaTER</b>	Cosmic Ray Telescope for the Effects of Radiation	<b>LDS</b>	Local Data Storage
<b>CSS</b>	Coarse Sun Sensor	<b>LEND</b>	Lunar Exploration Neutron Detector
<b>DET</b>	Direct-Energy-Transfer	<b>LFDB</b>	Liquid Fill and Drain valve-Bottom tank
<b>DLRE</b>	Diviner Lunar Radiometer Experiment	<b>LFDT</b>	Liquid Fill and Drain valve-Top tank
<b>DOD</b>	Depth of Discharge	<b>LHCP</b>	Left Hand Circular Polarization
<b>DOF</b>	Degree of Freedom	<b>LOI</b>	Lunar Orbit Injection
<b>DS</b>	Deep Space	<b>LOLA</b>	Lunar Orbiter Laser Altimeter
<b>DSB</b>	Data Storage Boards	<b>EPF</b>	Extended Payload Fairing
<b>DSN</b>	Deep Space Network	<b>LR</b>	Laser Ranging
<b>D/L</b>	Downlink	<b>LRO</b>	Lunar Reconnaissance Orbiter
<b>ECI</b>	Earth Centered Inertial	<b>LROC</b>	Lunar Reconnaissance Orbiter Camera
<b>EOL</b>	End of Life	<b>LTO</b>	Lunar Transfer Orbit
<b>EPS</b>	Electric Power System	<b>LV</b>	Launch Vehicle
<b>FOV</b>	Field Of View	<b>LVPC</b>	Low Voltage Power Converter
<b>FPGA</b>	Field Programmable Gate Array	<b>MA</b>	Mission Analysis
<b>GaAs</b>	Gallium Arsenide	<b>MAC</b>	Multi-Function Analog Card
<b>GFDP</b>	Gas Fill and Drain valve-Pyrovalve	<b>MAP</b>	Microwave Anisotropy Probe
<b>GFDR</b>	Gas Fill and Drain valve-Regulator	<b>MCC</b>	Mid Cruise Correction
<b>GFDT</b>	Gas Fill and Drain valve-Tank	<b>MEOP</b>	Maximum Expected Operating Pressure
<b>GG</b>	Gravity Gradient	<b>MIMU</b>	Miniature Inertial Measurement Unit
<b>GS</b>	Ground Station	<b>Mini-RF</b>	Mini Radio Frequency Technology Demonstration
		<b>MLI</b>	Multi Layer Insulator
		<b>MLV</b>	Manifold Latch Valve

<b>NEA</b>	Non Explosive Actuators	<b>SAM</b>	Solar Array Module
<b>NOI</b>	Nominal Orbit Injection	<b>SBC</b>	Single Board Computer
<b>NSI</b>	NASA Standard Initiators	<b>S/C</b>	Spacecraft
<b>OBDH</b>	OnBoard Data Handlng	<b>S/S</b>	Subsystem
<b>OM</b>	Output Module	<b>SNR</b>	Signal to Noise Ratio
<b>OQPSK</b>	Offset Quadrature Phase-Shift Keying	<b>SK</b>	Station Keeping
<b>OS</b>	Operating System	<b>SRP</b>	Solar Radiation Pressure
<b>OSR</b>	Optical Surface Reflector	<b>SSA</b>	Solid State Amplifier
<b>PCI</b>	Peripherical Component Interconnect	<b>SSR</b>	Solid State Recorder
<b>PDE</b>	Propulsion Deployment Electronics	<b>ST</b>	Star tracker
<b>PID</b>	Proportional Integral Derivative	<b>STDN</b>	Spacecraft Tracking and Data Network
<b>PMC</b>	PSE Monitor Card	<b>TCS</b>	Thermal Control System
<b>PS</b>	Propulsion System	<b>TLI</b>	Trans-Lunar Injection
<b>PSE</b>	Power Subsystem Electronics	<b>TLV</b>	Tank Latch Valve
<b>PSR</b>	Permanently Shadowed Region	<b>TOF</b>	Time of Flight
<b>PV</b>	PyroValve	<b>TRL</b>	Technology Readiness Level
<b>QPSK</b>	Quadrature Phase Shift Keying	<b>TTMTC</b>	Tracking Telemetry Telecommand System
<b>RAM</b>	Random Access Memory	<b>TWTA</b>	Traveling Wave Tube Amplifier
<b>RF</b>	Radio Frequency	<b>U/L</b>	Uplink
<b>RHCP</b>	Right Hand Circular Polarization	<b>USN</b>	Universal Space Network
<b>RW</b>	Reaction Wheel	<b>VDA</b>	Vapour Deposited Aluminum
<b>ROM</b>	Read Only Memory	<b>WS1</b>	White Sands 1
<b>SA</b>	Solar Array		

# Symbols

## Propulsion Subsystem

$I_{IJ}$	[kgm <sup>2</sup> ]	Inertia moment of I, J axes
$\Delta v$	[m/s]	Velocity variation
$\sigma$	[MPa]	Admissible Strength
$\rho$	[kg/m <sup>3</sup> ]	Density
$I_s$	[s]	Specific Impulse
$V$	[m <sup>3</sup> ]	Volume
$\gamma$	[–]	Specific Heat Ratio
R	[J/kgK]	Specific Gas Constant
$P_c$	[bar]	Chamber pressure

## TTMTC Subsystem

$\alpha_{enc}$	[–]	Spectrum utilization (related to encoding)
$\alpha_{mod}$	[–]	Spectrum utilization (related to modulation)
$D$	[m]	Diameter
$E_b/N_0$	[dB]	Energy per Bit to Noise density
$\beta_{mod}$	[deg]	Modulation Index
$B$	[Hz]	Bandwidth
$P_{carr}$	[W]	Carrier Power
$R$	[bit/s]	Data rate

## AOC Subsystem

$I_{IJ}$	[kg · m <sup>2</sup> ]	Inertia moment of I, J axes
$I_{max}$	[kg · m <sup>2</sup> ]	Maximum inertia moment
$I_{min}$	[kg · m <sup>2</sup> ]	Minimum inertia moment
$\mu$	[km <sup>3</sup> /s]	Moon's standard gravitational parameter
$R_{min}$	[km]	Nominal orbit radius
$\theta_{GG}$	[deg]	Maximum deviation angle
$F_s$	[W/m <sup>2</sup> ]	Solar irradiance
$c$	[m/s]	Speed of light in vacuum
$A_s$	[m <sup>2</sup> ]	Solar array surface
$q$	[–]	Reflective coefficient
$C_M$	[mm]	Center of Mass
$C_{SP}$	[mm]	Center of Solar Pressure
$T_{RW,disturbances}$	[Nm]	RW torque to counteract disturbances (BARF)
$T_{RW,slew}$	[Nm]	RW torque to achieve slew manoeuvre (BARF)
$T_{RW,yaw}$	[Nm]	RW torque to achieve yaw manoeuvre (BARF)
$\theta_{slew}$	[deg]	Slew manoeuvre angle
$\theta_{yaw}$	[deg]	Yaw manoeuvre angle
$t_{slew}$	[s]	Time required for slew manoeuvre
$t_{yaw}$	[s]	Time required for yaw manoeuvre
$h_{RW,required}$	[Nms]	RW angular momentum storage during one orbital period (BARF)
$h_{RW,capacity}$	[Nms]	RW angular momentum storage capacity (BARF)
$N_{orbits,desaturation}$	[–]	Number of orbits for RW to reach a saturation condition
$T_{desaturation}$	[days]	Time elapsed for RW to reach a saturation condition
$F_{th}$	[N]	Minimum thrust to achieve controllability
$t_{burn}$	[s]	Angular momentum dump burn length
$t_{burn,tot}$	[s]	Total angular momentum dump burn time
$I_{SP}$	[s]	Thrusters specific impulse
$N_{burns}$	[–]	Number of burns
$M_{desat}$	[kg]	Propellant mass needed for desaturation
$M_{SK}$	[kg]	Propellant mass needed for SK

## TC Subsystem

$\alpha$	[–]	Visible Absorbance
$\epsilon$	[–]	Infrared Emissivity
$T_{min}$	[°C]	Minimum admissible temperature
$T_{max}$	[°C]	Maximum admissible temperature
$\beta$	[deg]	Beta Angle
$R_{moon}$	[km]	Moon Radius
$\dot{q}$	[W/m <sup>2</sup> ]	Heat flux

$\dot{Q}$	[W]	Thermal Power
$A$	[ $m^2$ ]	Surface Area
<b>EP Subsystem</b>		
$I_{IJ}$	[ $kg \cdot m^2$ ]	Inertia moment of I, J axes
$\varepsilon_{BOL}$	[–]	Efficiency at Begin of Life
$I_d$	[–]	Inherent Degradation
$dpy$	[1/year]	Degradation per year
$I_0$	[ $W/m^2$ ]	Sun irradiance
$E_m$	[ $Wh/kg$ ]	Specific Energy
$E_v$	[ $Wh/dm^3$ ]	Energy Density
$\eta$	[–]	Battery line efficiency
$T_{daylight}$	[s]	Time spent in daylight during one orbit
$T_{eclipse}$	[s]	Time spent in eclipse during one orbit
$T_{life}$	[year]	Spacecraft lifetime
$P_D$	[W]	SA power request in daylight
$P_E$	[W]	SA power request in eclipse
$P_{BOL}$	[ $W/m^2$ ]	SA specific power produced at Begin of Life conditions
$P_{EOL}$	[ $W/m^2$ ]	SA specific power produced at End of Life conditions
$P_{SA}$	[W]	SA power demand
$A_{SA,real}$	[ $m^2$ ]	SA surface
$M_{SA}$	[kg]	SA mass
$N_{cells}$	[–]	Number of SA cells needed
$N_{strings}$	[–]	Number of SA strings needed
$N_{modules}$	[–]	Number of SA modules
$N_{series}$	[–]	Number of SA cells in series needed to form a string
$N_{parallel}$	[–]	Number of battery cells composing a layer
$N_{cells,series}$	[–]	Number of battery cells to put in series to obtain the desired voltage
$T_R$	[h]	Time window in which battery must provide power
$P_R$	[W]	Power required for the most critical mode (battery)
$M_{battery}$	[kg]	Battery Mass
$V_{battery}$	[ $dm^3$ ]	Battery Volume
$V_{real}$	[V]	Actual battery voltage obtained
$C_{req}$	[Wh]	Required capacity to fulfill the power demand
$C_{string}$	[Wh]	Single battery string capacity
$C_{real}$	[Wh]	Actual battery system capacity
$\beta$	[deg]	Angle between a satellite plane and the mooncentric position of the Sun
<b>Miscellaneous</b>		
$C_3$	[ $km^2/s^2$ ]	Characteristic energy of a LV

## APPENDIX

Component	Mass	Source
<b>PS</b>		
Propellant tanks	61.6	CAD
Tank structural interface	85.9	CAD
Pressurant tank armature	7.1	CAD
Pressurant tank	15.7	CAD
ACS thrusters	2.4	[15]
Injection thrusters	4.5	[14]
Feeding systems and cables	17.7	Margin [18]
<b>TTMTC</b>		
HGA	3.6	Model [18]
Omnidirectional antenna	0.5	Model [18]
Ka-band system	8.4	[4]
S-band system	8.8	[4]
Cables	2.1	Margin [18]
<b>AOCS</b>		
Star trackers	5.2	[38]
MIMU	4.6	[39]
Coarse Sun Sensors	0.011	[4]
Reaction Wheels	47.6	[4]
Propulsion Deployment Electronics	9.4	[4]
<b>TCS</b>		
Sensors	2.4	[40]
Heaters	0.4	[40]
Hardware	5.2	[40]
MLI	18.9	[40]
<b>EPS</b>		
Battery	30.9	Model [18]
Solar array	34.3	Model [18]
Power System Electronics	3.0	Estimated
Cables	6.8	Margin [18]
<b>OBDH</b>		
System assembly	20.9	[61]
Cables	2.1	Margin [18]
<b>Payload</b>		
LOLA	4.4	[31]
CRaTER	5.6	[62]
LROC	18.5	[63]
LEND	26.3	[64]
DLRE	6.5	[65] [66]
LAMP	4.0	[67]
Mini-RF	13.9	[68]
<b>Structure</b>		
Skin	70.1	CAD
Baseplate	36.9	CAD
Reaction Wheels armature	31.5	CAD
Star trackers armature	2.9	CAD

Dry mass	630.6	kg
Propellant mass	1039.0	kg
Pressurant mass	4.5	kg
Total launch mass	1674.2	kg

Table 9: CAD masses approximations